



TECHNISCHE
UNIVERSITÄT
WIEN



Diploma Thesis

Numerical investigations on heat transfer in a fast firing brick kiln

carried out for the purpose of obtaining the degree of

Diplom-Ingenieur

submitted at TU Wien, Faculty of Mechanical and Industrial
Engineering,

by

Stefan Gutschka

Matr.Nr.: 01328882

under the supervision of

Privatdoz. Dipl.-Ing. Dr.techn. Christoph Reichl
Institute of Fluid Mechanics and Heat Transfer

Dipl.-Ing. Dr.techn. Julian Unterluggauer
Sustainable Thermal Energy Systems, AIT Austrian Institute of
Technology GmbH

Vienna, 21.9.2024



TECHNISCHE
UNIVERSITÄT
WIEN

Ich habe zur Kenntnis genommen, dass ich zur Drucklegung meiner Arbeit unter der Bezeichnung

Diplomarbeit

nur mit Bewilligung der Prüfungskommission berechtigt bin.

Ich erkläre weiters an Eides statt, dass ich meine Diplomarbeit nach den anerkannten Grundsätzen für wissenschaftliche Abhandlungen selbständig ausgeführt habe und alle verwendeten Hilfsmittel, insbesondere die zugrunde gelegte Literatur genannt habe.

Weiters erkläre ich, dass ich dieses Diplomarbeitsthema bisher weder im In- noch Ausland (einer Beurteilerin/einem Beurteiler zur Begutachtung) in irgendeiner Form als Prüfungsarbeit vorgelegt habe und dass diese Arbeit mit der vom Begutachter beurteilten Arbeit übereinstimmt.

Wien, am 21.9.2024

Acknowledgements

First and foremost, I extend my sincere thanks to my advisors, Christoph Reichl and Julian Unterluggauer, whose expertise, patience, and encouragement guided me through each stage of this research.

I would also like to thank all my colleagues at AIT who made my time there very enjoyable and fun.

A heartfelt thank you to my family, whose unconditional love and encouragement have been a constant source of strength throughout my academic journey. Last but not least I want to thanks to Hannah, without her, I would not have been where I am now.

This work has been conducted within the project „GreenBricks“ (FFG no. 999894581). The project is supported with funds from the Climate and Energy Fund and implemented in the framework of the RTI-initiative “Flagship region Energy”.

Kurzfassung

In dieser Arbeit werden die Wärmeübertragungsmechanismen in einem Schnellbrandofen, einer kritischen Komponente im Ziegelherstellungsprozess, untersucht. Tunnelöfen, die in der Keramikindustrie für die Herstellung von Grobkeramik wie Ziegeln weit verbreitet sind, arbeiten in einem kontinuierlichen Prozess, bei dem die Ofenwagen Ziegel durch verschiedene Zonen transportieren. Um den CO_2 -Ausstoß beim Brennen von Ziegeln zu verringern, muss die Wärmeübertragung innerhalb des Ofens verbessert werden. Der Wirkungsgrad der Wärmeübertragung innerhalb dieser Zonen ist entscheidend für den Gesamtenergieverbrauch und die Qualität des Endprodukts. Daher werden eine Reihe von CFD-Simulationen mit verschiedenen Modellen und Einstellungen durchgeführt, um die Frage zu beantworten, ob es vorteilhaft ist, die Decke im Inneren des gegebenen schnell brennenden Ziegelofens abzusenken. Wie man sieht, hat die Platzierung der Ziegel im Ofen einen erheblichen Einfluss auf die Wärmeübertragung und kann leichter verändert werden als die Geometrie des Ofens selbst. Das Absenken der Decke im Ofen würde, verglichen mit der Änderung der Anordnung der Ziegel auf den Ofenwagen, kostspielige Änderungen nach sich ziehen. Die Ergebnisse der Simulationen werden auch mit den zur Verfügung gestellten experimentellen Daten validiert, die durch die Messung der verschiedenen Ziegel- und Lufttemperaturen gesammelt wurden. Die unterschiedliche Platzierung der Steine in den erstellten Modellen kann als Ausgangspunkt für künftige Untersuchungen zur weiteren Steigerung der Effizienz dienen.

Abstract

This thesis investigates the heat transfer mechanisms within a fast-firing tunnel kiln, a critical component in the brick manufacturing process. Tunnel kilns, widely used in the ceramics industry for the production of coarse ceramics such as bricks, operate through a continuous process where kiln cars transport goods through distinct zones. In order to reduce the CO_2 emitted by the brick burning process, the heat transfer inside the kiln has to be improved. The efficiencies of the heat transfer within these zones are crucial for the overall energy consumption and the quality of the final product. Thus, a series of CFD simulations with different models and setups are carried out in order to answer the question if it is advantageous to lower the ceiling inside the given fast firing brick kiln. As can be seen, the placement of the bricks inside the kiln has a significant impact on the heat transfer and can be altered more easily than changing the geometry of the kiln itself. Lowering the ceiling inside the kiln would involve expensive modifications compared to changing the mount of the bricks on the kiln cars. The results of the simulations are also validated with provided experimental data collected by measurement of different brick and air temperatures. Different placement of bricks in the generated models can be used as a starting point for future investigations to further increase the efficiency.

Nomenclature

Abbreviations

AIT	Austrian Institute Of Technology
CFD	Computational Fluid Dynamics
GCI	Grid Convergence Index
RANS	Reynolds Averaged Navier Stokes
S2S	Surface To Surface
UDF	User Defined Function

Greek Symbols

α	Heat Transfer Coefficient	$W/(m^2K)$
ϵ	Dissipation Rate Of Turbulent Kinetic Energy	m^2/s^3
μ	Dynamic Viscosity	Pa s
ν	Kinematic Viscosity	m^2/s
ν_t	Turbulent Viscosity	m^2/s
ϕ	Extrapolated Value	
ρ	Density	kg/m^3
τ_w	Wall Shear Stress	N/m^2
θ	Angle	rad

Latin Symbols

\dot{m}	Mass Flow Rate	kg/s
-----------	----------------	--------

Nomenclature

\dot{Q}	Heat Flow Rate	W
\dot{V}	Volumetric Flow Rate	m ³ /s
\dot{W}	Power	W
\vec{u}	Velocity vector	m/s
\vec{x}	Cartesian Direction Vector	m
A	Area	m ²
c_p	Specific Heat Capacity At Constant Pressure	J/(kg K)
d	Diameter	m
D_h	Hydraulic Diameter	m
e	Relative Error	%
h	Representative Grid Size	m
k	Turbulent Kinetic Energy	J/kg
L, l	Length	m
m	Mass	kg
M_w	Molecular Weight	kg/mol
P	Power	W
p	Pressure	Pa or bar
p_c	Order Of Convergence	1
R	Universal Gas Constant	J/(kg K)
r	Radius	m

Nomenclature

R_c	Convergence Ratio	1
r_g	Grid Refinement Ratio	1
Re	Reynolds Number	1
T	Temperature	K
t	Time	s
u, v, w	Cartesian Components of Velocity vector	m/s
V	Volume	m ³
x, y, z	Cartesian Coordinates	m

Subscripts

avg	Average
eff	Effective
i,j,k	Indices For The Tensor Notation
in	Inflow
max	Maximal
min	Minimal
out	Outflow

Contents

1	Introduction	1
2	Theoretical Background	2
2.1	Fast firing brick kiln	2
2.2	Laminar and turbulent flows	5
2.3	Turbulence modeling	6
2.4	Surface to surface radiation	8
2.5	Grid independence	11
2.5.1	Richardson Extrapolation	11
2.5.2	Grid convergence index	11
2.6	Effective alpha	14
3	Numerical Setup & Methodology	15
3.1	Overview	15
3.1.1	Used solver solution methods	17
3.1.2	Used Models	18
3.1.3	Materials properties	18
3.2	Grid independence	20
3.3	Boundary conditions	24
3.3.1	Temperature and velocity scaling	28
4	Results & Discussion	31
4.1	Pressure Drop	45
4.2	Validation	48
5	Conclusion & Future Research	51
	References	56
	Appendix A Total heat flux over time	58

Appendix B Temperature contour plots

59

1 Introduction

In times of climate changes and high energy prices, it is crucial to save as much energy and CO₂ emissions as possible. In case of bricks, the costs for thermal energy needed for production and distribution account for 25 to 35% of the overall cost of one brick. There are many different kinds of kilns which can be used in order to produce bricks, but here only fast firing kilns are considered. There are many different areas of improvement to reach a optimal configuration for example the sealing of the kiln, placement of the bricks on the kiln cars and larger pressure drops along the kiln. In order to reach shorter firing times, which is a direct measure of the kiln efficiency for the firing process. This means the faster a brick can be fired to acceptable quality, the lower the thermal energy consumption rate will be. This leads to a overall lower energy consumption, which can lower the operational cost significantly as well as saves CO₂ emission. Most of these kilns are fired with gas, but also a heating with electricity is possible and could lower the CO₂ footprint of the brick production. Bricks are in stiff competition with other building materials because they are more cost intensive to produce, as they need preparation of the raw material and involve a drying and firing process (Vogt (2017a)). However, with a careful optimization or development of the next generation of kilns in combination with the usage of green energy this could give them the edge over all other building material.

2 Theoretical Background

2.1 Fast firing brick kiln

A fast firing brick kiln is a form of tunnel car kiln, which is often used in the ceramics industry, especially for coarse ceramics such as bricks. The firing process involves loading the goods onto kiln cars, which are then continuously pushed through the kiln. The cars pass through three different zones, the first zone being the preheating zone, where it is heated. Then it passes through a firing zone where the good is heated up to the required temperature. At these high temperatures, sintering occurs and imparts the desired product properties. After the firing zone, the load enters the cooling zone, where ambient air cools the goods. The cooling rate is adjusted according to the sensitivity of cooling cracks of the sintered good (Specht (2014)). As the specific kiln losses rise with increasing firing time, which is not only due to a relative increase of insulation losses but due to the outdated technical status of kilns with long firing time (Vogt (2017a)). Therefore, it is important to get short firing times for the efficient use of a kiln.

2 Theoretical Background

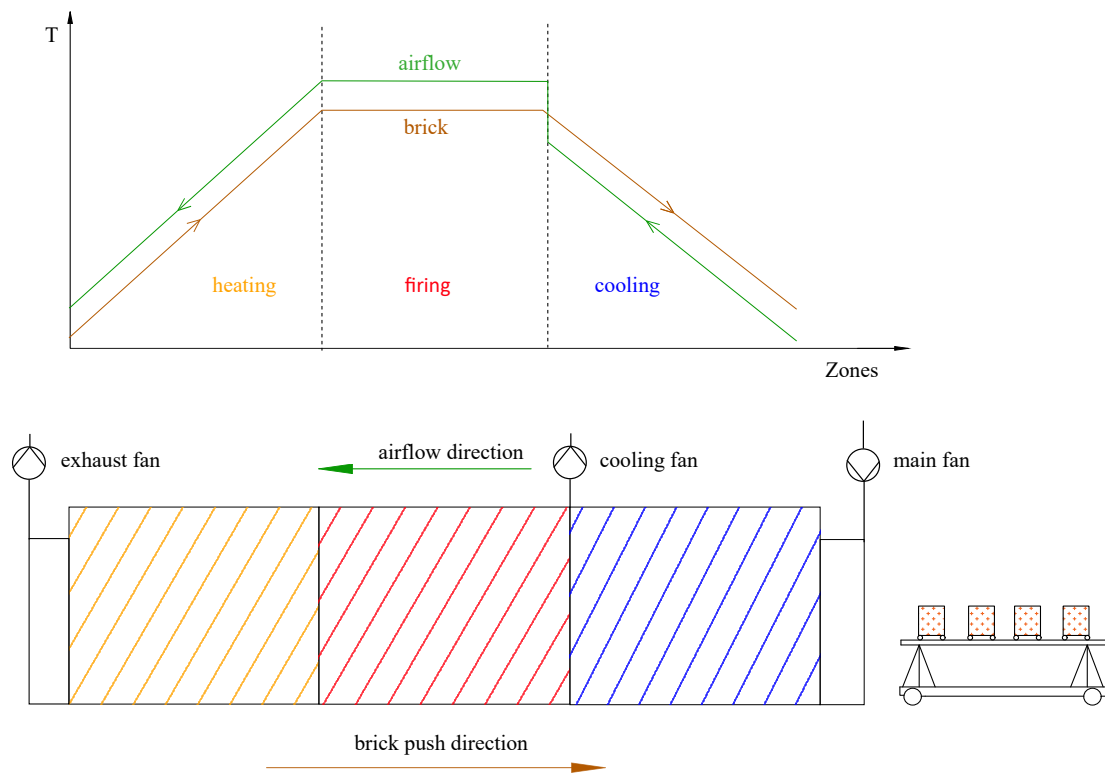


Figure 1: Principals of a fast firing brick kiln.

With fast firing brick kilns, there is a general lack of new developments, although there are various areas of improvement.

- In order to achieve the highest possible heat transfer, the bricks should be placed tight together onto the cars.

2 Theoretical Background

- Forced convection is the most important heat transfer mechanism. This enables the direct control by manipulating the mass flow in each zone. In order to reach the maximum heat transfer possible, the required mass flow would result in an to high pressure drops along the kiln.
- In order to maximize the effective heat transfer coefficient, the pressure drop along the kiln should also be maximized within the possible limits of the fans.
- To make these larger pressure drops possible, the kiln needs better sealing.
- To minimize the amount of gas passing through the kiln without contact to the bricks, the edge gap should be as small as possible or profiled with spoiler bars.

In order to achieve the shortest firing time possible, all parameters should be handled in a way that the maximum permissible stresses resulting from differential temperatures and diffusion processes are not exceeded. Another possibility to further decrease the energy consumption is to eliminate the kiln cars, which are responsible for about 9% of the total energy loss (Vogt (2017a)). All energy losses can be seen in 2 and notably kiln cars and insulation losses are a big part of them with around 18%.

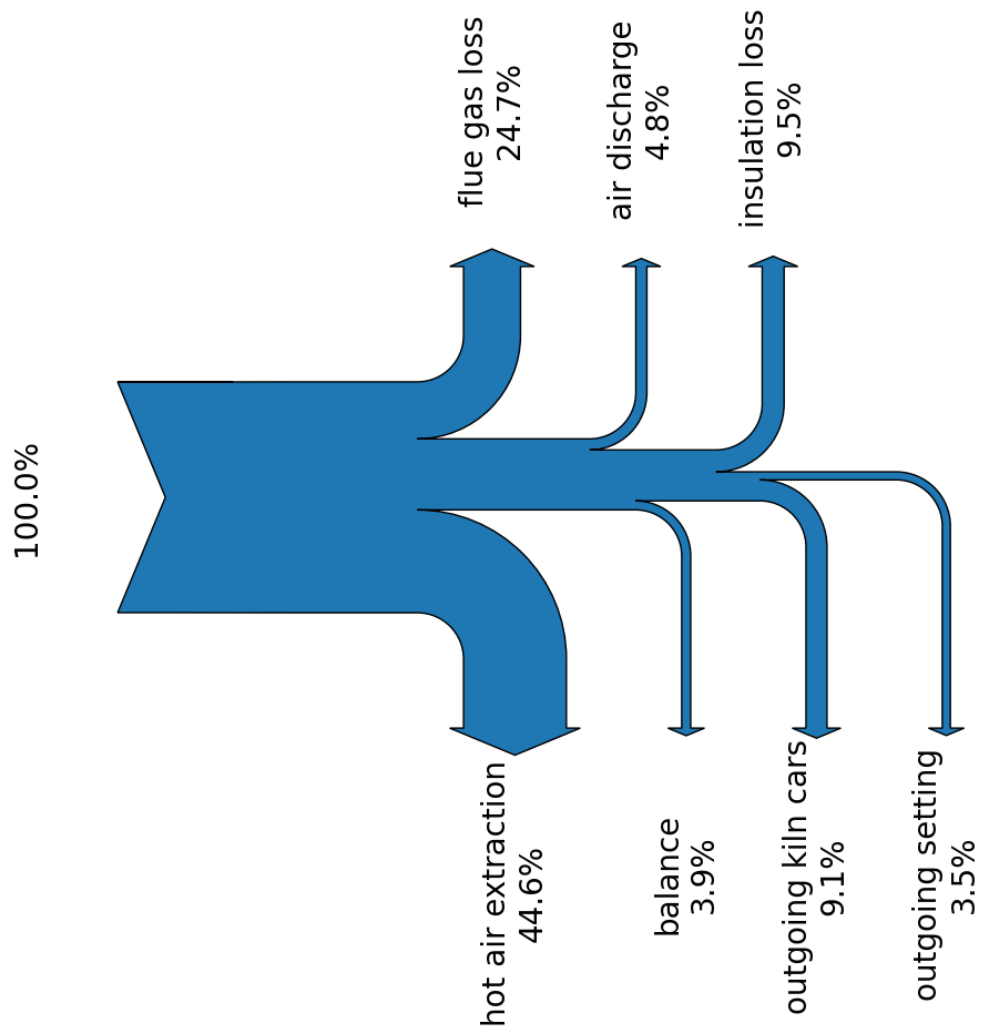


Figure 2: Sankey diagram of mean energy balance[Vogt (2017b)]

2.2 Laminar and turbulent flows

In order to distinguish between different flow regimes, the Reynolds number can be used. The following definition

$$Re = \frac{uD_h}{\nu} \quad (1)$$

where u is the stream wise mean velocity, D_h is the hydraulic diameter formed in the case of rectangular cross-section by $D_h = \frac{2ab}{a+b}$ and ν the kinematic viscosity is used. In case of pipe flows the critical Reynolds number below, which the flow is considered laminar is around $Re = 2300$, for flow around a flat plate the critical Reynolds number is $Re = 500000$. In our case, which is more on the pipe side, the cross-section is not a circle but a rectangle. Therefore, the hydraulic diameter described above is used to form the Reynolds number.

2.3 Turbulence modeling

The most common approach to model turbulence is the usage of the RANS (*Reynolds Averaged Navier–Stokes*) in combination with some modeling to close the system of equations. The RANS equations are obtained by decomposing a quantity ϕ into a mean component $\bar{\phi}$ and a fluctuating component ϕ' , where the mean component can be expressed as

$$\bar{\phi}(\vec{x}, t) = \lim_{t \rightarrow \infty} \frac{1}{t_{avg}} \int_t^{t+t_{avg}} \phi(\vec{x}, t') dt'. \quad (2)$$

This Reynolds averaging is then applied onto the Navier-Stokes equation and the equation of the mean quantities can be written as

$$\rho(\vec{u} \cdot \nabla) \bar{u}_i = -\frac{\partial \bar{p}}{\partial x_i} + \frac{\partial}{\partial x_j} \left[\bar{\tau}_{ij} - \overline{\rho u'_i u'_j} \right] \quad (3)$$

Here $\bar{\tau}_{ij}$ represents the viscous stress and $\tau_{ij}^R - \overline{\rho u'_i u'_j}$. This system of equations can't be solved directly because it's an under-determined system and therefore some modeling is required, which leads to two additional transport equations for k and ω (Ciofalo (2022)). The following formulation has small modifications proposed by Menter (Menter (2009)) in contrast to the original formulation (Menter (1994)).

$$\begin{aligned} \frac{\partial \rho k}{\partial t} + \frac{\partial \rho \bar{u}_i k}{\partial x_i} &= \frac{\partial}{\partial x_i} \left[(\mu + \sigma_k \mu_t) \frac{\partial k}{\partial x_i} \right] + \tilde{P}_k - \beta^* \rho k \omega \\ \frac{\partial \rho \omega}{\partial t} + \frac{\partial \rho \bar{u}_i \omega}{\partial x_i} &= \frac{\partial}{\partial x_i} \left[(\mu + \sigma_\omega \mu_t) \frac{\partial \omega}{\partial x_i} \right] + \alpha \frac{1}{\nu_t} \tilde{P}_k - \beta \rho \omega^2 + 2(1 - F_1) \rho \frac{\sigma_\omega}{\omega} \frac{\partial k}{\partial x_i} \frac{\partial \omega}{\partial x_i} \\ \nu_t &= \frac{a_1 k}{\max(a_1 \omega, S F_2)}; S = \sqrt{2 S_{ij} S_{ij}} \\ P_k &= \mu_t \frac{\partial \bar{u}_i}{\partial x_j} \left(\frac{\partial \bar{u}_i}{\partial x_j} \frac{\partial \bar{u}_j}{\partial x_i} \right) \\ \tilde{P}_k &= \min(P_k, 10 \beta^* \rho k \omega) \\ F_1 &= \tanh \left(\left[\min \left(\max \left(\frac{\sqrt{k}}{\beta^* \omega y}, \frac{500 \nu}{y^2 \omega}, \frac{4 \rho \sigma_\omega k}{C D_{k\omega} y^2} \right) \right] \right)^4 \right) \\ F_2 &= \tanh \left(\left[\max \left(\frac{2 \sqrt{k}}{\beta^* \omega y}, \frac{500 \nu}{y^2 \omega} \right) \right]^2 \right) \\ C D_{k\omega} &= \max \left(2 \rho \sigma_\omega \frac{1}{\omega} \frac{\partial k}{\partial x_i} \frac{\partial \omega}{\partial x_i}, 10^{-10} \right) \end{aligned}$$

For the used constants, a blend between the constants of the $k - \epsilon$ model and the $k - \omega$ model is used in the form of $\alpha = \alpha_1 F_1 + \alpha_2 (1 - F_1)$. The function F_1 is a blending function, which ranges from 1 at the wall to 0 at the free stream. In order to achieve an accurate near-wall modeling of the standard two-layer approach for fine near-wall meshes ($y^+ \approx 1$) and wall-function meshes ($y^+ \approx 30$) at the same time, enhanced wall functions are used. Here y^+ is defined as,

$$\begin{aligned} y^+ &= \frac{\rho u_\tau y}{\mu} \\ u_\tau &= \sqrt{\frac{\tau_w}{\rho h o_w}} \end{aligned}$$

where u_τ is the friction velocity and y is the distance to the all.

2.4 Surface to surface radiation

In order to describe the exchange of radiative energy between enclosed gray diffuse surfaces, the $S2S$ radiation model is used. The main assumptions of this model are:

- surfaces are rough, which means that the intensity of the radiation leaving the surface is angle dependent
- Surfaces have uniform radiosity, which means that the total radiation leaving a surface (emitted and reflected radiation), is assumed to be uniform across the entire surface and equally in all directions.
- Surfaces emit radiation based on their temperature, with the intensity varying by direction and wavelength. The maximum radiation a surface can emit is equivalent to that of a black body at the same temperature, known as a black surface. Most surfaces emit less radiation than a black body. If a surface emits a consistent fraction of the black body radiation across all wavelengths, it is called a gray surface. However, if the fraction varies with wavelength, it is referred to as a non-gray surface. For this model, all surfaces are assumed gray.

The radiation interchange between two area elements is shown in Fig(3) where $I_i = J_i/\pi$ and $I_j = J_j/\pi$ are the intensity of radiation leaving dA_j and dA_i . J_i, J_j are the radiosity of the area elements dA_j, dA_i which is assumed uniform. (Venkateshan (2021)).

The total power leaving dA_j is

$$dP_j = J_j dA_j = \pi I_j dA_j \quad (6)$$

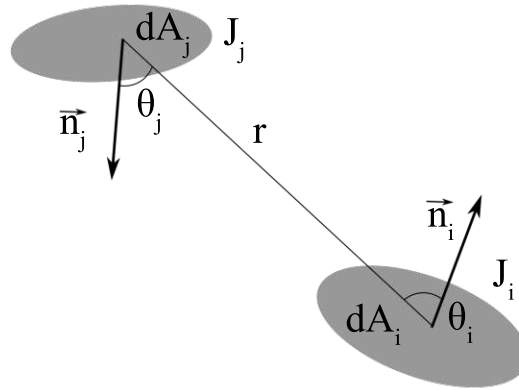


Figure 3: radiant interchange between two area elements [Venkateshan (2021)]

and the power incident on dA_i from the total power leaving dA_j is

$$dP_i = I_j dA_j \cos \theta_j d\Omega \quad (7)$$

where $d\Omega$ is the solid angle subtended by dA_i at dA_j which is given by $d\Omega = \frac{\cos \theta_i dA_i}{r^2}$. The length of the line joining the midpoints of dA_i and dA_j is r .

The ratio $\frac{dP_i}{dP_j}$ can be obtained and is given by,

$$\frac{dP_i}{dP_j} = \frac{\cos \theta_i \cos \theta_j dA_i}{\pi r^2} = F_{dA_i-dA_j} \quad (8)$$

which is a geometric parameter and is called view factor. Using the relation $dA_i \times F_{dA_i-dA_j} = dA_j \times F_{dA_j-dA_i}$ and integrating over both areas leads to

$$F_{ij} = \frac{1}{A_i} \int_{A_i} \int_{A_j} \frac{\cos \theta_i \cos \theta_j}{\pi r^2} dA_i dA_j \quad (9)$$

The energy leaving from a surface k is

$$q_{out,k} = \epsilon_k \sigma T_k^4 + \rho_k q_{in,k} \quad (10)$$

where $q_{out,k}$ is the energy flux leaving the surface, ϵ_k is the emissivity, σ is the Stefan-Boltzmann constant and $q_{in,k}$ is the energy flux incident on the surface

from the surrounding. The incident energy flux $q_{in,k}$ can be expressed in terms of energy flux leaving all other surfaces

$$A_k q_{in,k} = \sum_{j=1}^N A_j q_{out,j} F_{jk} \quad (11)$$

If we plug this into Equation(10) we obtain

$$q_{out,k} = \epsilon_k \sigma T_k^4 + \rho_k \sum_{j=1}^N q_{out,j} F_{kj} \quad (12)$$

This can finally be rewritten in the form

$$J_k = E_k + \rho_k \sum_{j=1}^N F_{kj} J_j \quad (13)$$

which can be recast into matrix form

$$KJ = E \quad (14)$$

where J is the radiosity vector, E the emissive power vector and K a $N \times N$ matrix.

These calculations can get very expensive for large numbers of surfaces. To reduce the computation time, surfaces are gathered together with their neighbors in clusters. These clusters are made by starting from a face and adding their neighbors until a specified number of faces per cluster is reached. These Clusters are then used to calculate the necessary view factors (ANSYS (2023)). The view factors are only once necessary to calculate if the geometry is unchanged.

2.5 Grid independence

2.5.1 Richardson Extrapolation

The generalized Richardson Extrapolation is

$$f_{exact} \simeq f_1 + \frac{(f_2 - f_1)}{(r^p - 1)} \quad (15)$$

with order p and grid ratio $r_g = \frac{h_2}{h_1}$, where h_1 and h_2 are the grid spacing of two different grids. As can be easily seen in Equation(15) the correction to the grid solution f_1 is an error estimation, which can be expressed as

$$E_1 = \frac{\epsilon}{r^p - 1} \quad (16a)$$

$$\epsilon = \frac{f_2 - f_1}{f_1} \quad (16b)$$

For $E_1 \ll 1$ this is a good approximation but not in general because ϵ does not take r or p into account (Roache (1994)).

2.5.2 Grid convergence index

The error estimator E_1 does not give a bound on the error but just an error band and also does not has a very good confidence interval. Therefore, the grid convergence index was introduced, which relates a ϵ -value obtained with p_c and r_g in a grid refinement study to that study of the same problem with $p_c = 2$ and $r_g = 2$.

$$GCI = \frac{3|\epsilon|}{(r^p - 1)} \quad (17)$$

The value of 3 can be considered a very conservative factor and should only be used if only two different grids are considered. In the case of three different grids, a factor of 1.25 is proposed.(Celik et al. (2008))

In order to carry out a grid independence study, the following methodology proposed in Celik et al. (2008) will be used. This method can be divided into five steps.

1. Define a representative cell h for the tree-dimensional case

$$h = \left[\frac{1}{N} \sum_{i=1}^N \Delta V_i \right]^{\frac{1}{3}} \quad (18)$$

2. Select three significantly different sets of grids that are significantly different.
In this case, that means that for, the refinement factor

$$r_g = h_{corse}/h_{fine} \geq 1.3$$

holds.

3. Calculate equation (19) using fixed-point iteration

$$p_c = \frac{1}{\ln r_{21}} |\ln |\epsilon_{32}/\epsilon_{21}| + q(p)| \quad (19a)$$

$$q(p_c) = \ln \frac{r_{21}^p - s}{r_{32}^p - s} \quad (19b)$$

$$s = \text{sign}(\epsilon_{32}/\epsilon_{21}) \quad (19c)$$

4. Calculate extrapolated values

$$\phi_{ext}^{21} = \frac{(r_{21}^p \phi_1 - \phi_2)}{(r_{21}^p - 1)} \quad (20)$$

5. Calculate the following error estimates

$$\text{approximate relative error} \quad e_a^{21} = \left| \frac{\phi_1 - \phi_2}{\phi_1} \right| \quad (21a)$$

$$\text{extrapolated relative error} \quad e_{ext}^{21} = \left| \frac{\phi_{ext}^{12} - \phi_1}{\phi_{ext}^{12}} \right| \quad (21b)$$

$$\text{grid convergence index} \quad GCI_{fine}^{21} = \frac{1.25e_a^{21}}{r_{21}^p - 1} \quad (21c)$$

2 Theoretical Background

In order to obtain the convergent condition of the system, the convergence ratio $R_c = \epsilon_{21}/\epsilon_{32}$ can be used. There are three different possible convergence conditions, which are

1. monotonic convergence $0 < R_c < 1$
2. oscillatory convergence $R_c < 0$
3. divergence $R_c > 1$

according to Mat Ali et al. (2009).

2.6 Effective alpha

In order to calculate a heat transfer coefficient, the approach of an effective alpha is used (Schröder (1971), Jeschar (1990), Vogt (1991)). The position of the temperature T_{L1} and T_{L2} are taken at a plane 5 cm before and 5 cm after the brick, and then mass flow averaged according to Equation(22b) and Equation(22c).

$$\alpha_{eff} = \frac{\dot{m}c_p}{A} \ln \frac{\bar{T}_Z(t) - \bar{T}_{L1}(t)}{\bar{T}_Z(t) - \bar{T}_{L2}(t)} \quad (22a)$$

$$\bar{T}_{L1}(t) = \frac{1}{\dot{m}} \int T_{L1}(t) d\dot{m} \quad (22b)$$

$$\bar{T}_{L2}(t) = \frac{1}{\dot{m}} \int T_{L2}(t) d\dot{m} \quad (22c)$$

$$\bar{T}_Z(t) = \frac{1}{V} \int T_Z(t) dV \quad (22d)$$

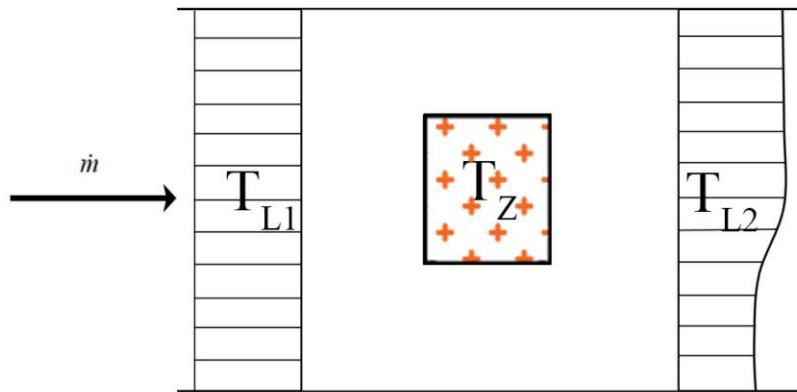


Figure 4: Temperatures used in α_{eff} calculation.

3 Numerical Setup & Methodology

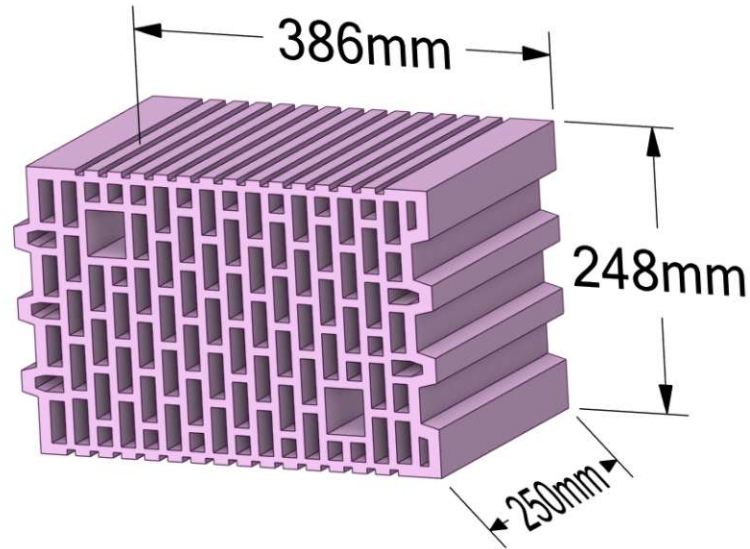


Figure 5: Dimensions of one single brick.

3.1 Overview

There are many cases and setups considered, which are described briefly. The simulation time in all the cases listed in Table(1) was $t = 7200s$ and the time step used $\Delta t = 0.2s$. Each time step had a maximum of 6 iterations. The height of the domain over the brick was reduced by about 75% between the large and small cases.

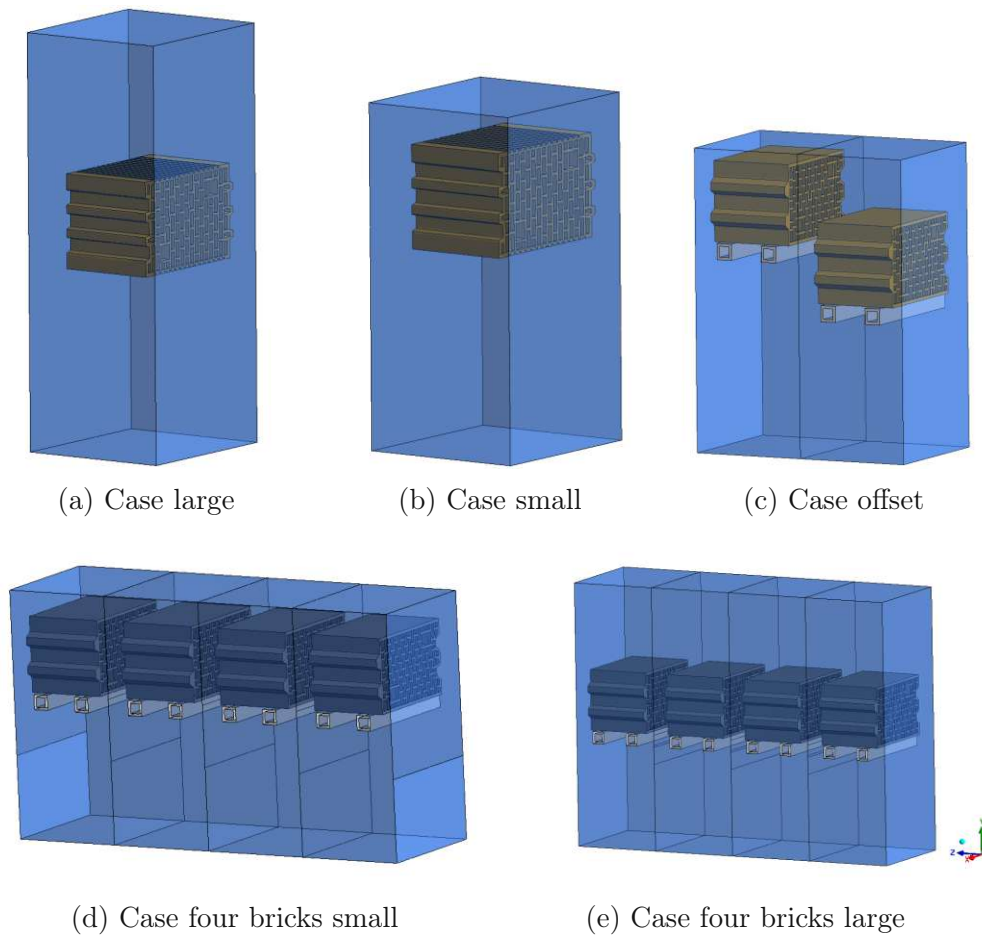


Figure 6: Overview over all different used geometries

Table 1: Overview of different cases

case name	bricks	inlet type	mass flow (kg/s)
small first approach	1	mass flow inlet	0.4 0.6
large first approach	1	mass flow inlet	0.4 0.6
4 bricks small	4	velocity inlet	0.4 0.6
4 bricks large	4	velocity inlet	0.4 0.6
4 bricks smaller inlet small	4	velocity inlet	0.4
4 bricks smaller inlet large	4	velocity inlet	0.4
4 bricks offset	4	velocity inlet	0.4
validation	4	velocity inlet	0.4

Table 2: Dimensions of the different cases

case name	L(z-dir)xB(x-dir)xH(y-dir)(mm)	figure
small first approach	400×446×825	6b
large first approach	400×446×1095	6e
4 bricks small	1428×446×825	6d
4 bricks large	1428×446×1095	6e
4 bricks smaller inlet small	1428×446×825	6d
4 bricks smaller inlet large	1428×446×1095	6e
4 bricks offset	1428×446×945	6c
validation	1785×446×945	6c
GCI	357×446×825	6b

3.1.1 Used solver solution methods

Here, the used solution methods can be seen in Table(3). These methods are used for all different cases described in 1. For every spatial discretization, a second-order scheme is used and for temporal discretization, a first-order implicit scheme is used. When second order upwind is used, a value at a cell face is evaluated by $\phi_f = \phi + \nabla\phi\vec{r}$ where \vec{r} is the vector from the upstream cell centroid to the face centroid. The gradient $\nabla\phi$ is evaluated using the least squares cell-based formulation $\nabla\phi_{c0}\Delta\vec{r}_i = \phi_{ci} - \phi_{c0}$ on all surrounding cells⁷. This leads to the simple form of, $\mathbf{J}\nabla\phi_{c0} = \Delta\phi$ where \mathbf{J} is a pure geometric coefficient matrix.

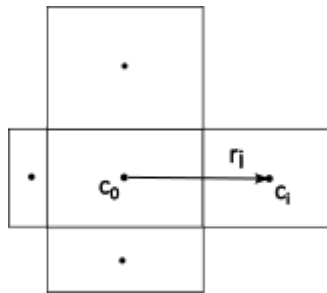


Figure 7: Evaluation of a gradient[ANSYS (2023)].

Table 3: Solution Methods

type	method
pressure-velocity coupling	SIMPLE
gradient	least squares cell based
pressure	second order central differences
density	second order upwind
momentum	second order upwind
turbulent kinetic energy	second order upwind
specific dissipation rate	second order upwind
energy	second order upwind
flux type	rhie-chow momentum based
transient formulation	first order implicit

3.1.2 Used Models

The models, which are used in all cases, are listed below (see Table 4). The energy model enables to solve the energy equation in the form

$$\frac{\partial}{\partial t} \left(\rho \left(e + \frac{u^2}{2} \right) \right) + \nabla \cdot \left(\rho u \left(h + \frac{u^2}{2} \right) \right) = \nabla \cdot (k_{eff} \nabla T - \sum_j h_j \vec{J}_j + \tau_{eff} \cdot \vec{v}) + S_h \quad (23)$$

where k_{eff} is the viscous conductivity, \vec{J}_j the diffusion flux, S_h the volumetric heat sources and the first three terms on the right side energy transfer due to conduction, specific diffusion and viscous dissipation respectively (ANSYS (2023)).

Table 4: Used models and solver type

models	solver	
energy	type	pressure-based
viscous $k - \omega SST$	velocity formulation	absolute
surface to surface radiation	time	transient

3.1.3 Materials properties

For the solid brick material, the following properties were used:

Table 5: Material properties

property	solid	fluid
density kg/m^2	1650	ideal gas
cp (specific heat) J/kgK	piecewise linear	nasa 9 picewise polynomial
thermal conductivity W/mK	0.265	kinetic theory
viscosity kg/ms	-	sutherland (three coefficient method)

As stated in Table(5) for the specific heat in solid a linear temperature dependence is assumed(see Figure(8b)). For the fluid, nasa 9 picewise polynomial is used, which solves

$$\frac{C_p^0(T)}{R} = a_0T^{-2} + a_1T^{-1} + a_2 + a_3T + a_4T^2 + a_5T^3 + a_6T^4 \quad (24)$$

for different coefficients a_i for different temperature regions, which leads to the curve plotted in Figure(8a). The viscosity of the fluid is modeled using a three coefficient sutherland method described by

$$\mu = \mu_0 \left(\frac{T}{T_0} \right)^{\frac{3}{2}} \frac{T_0 + S}{T + S} \quad (25)$$

where T is the static temperature, $S = 110.56K$ is the sutherland constant, $\mu_0 = 1.717 \cdot 10^{-5} \frac{kg}{ms}$ and $T_0 = 271.11K$ for moderate temperatures and pressures, see Figure(8c). When the density of the fluid is described by the ideal gas law, one can define the thermal conductivity with the kinetic theory as following:

$$k = \frac{15R}{4M_w} \mu \left[\frac{4c_p M_w}{15R} + \frac{1}{3} \right] \quad (26)$$

where R is the universal Gas constant, M_w the molecular weight, c_p the specific heat capacity and μ the dynamic viscosity.

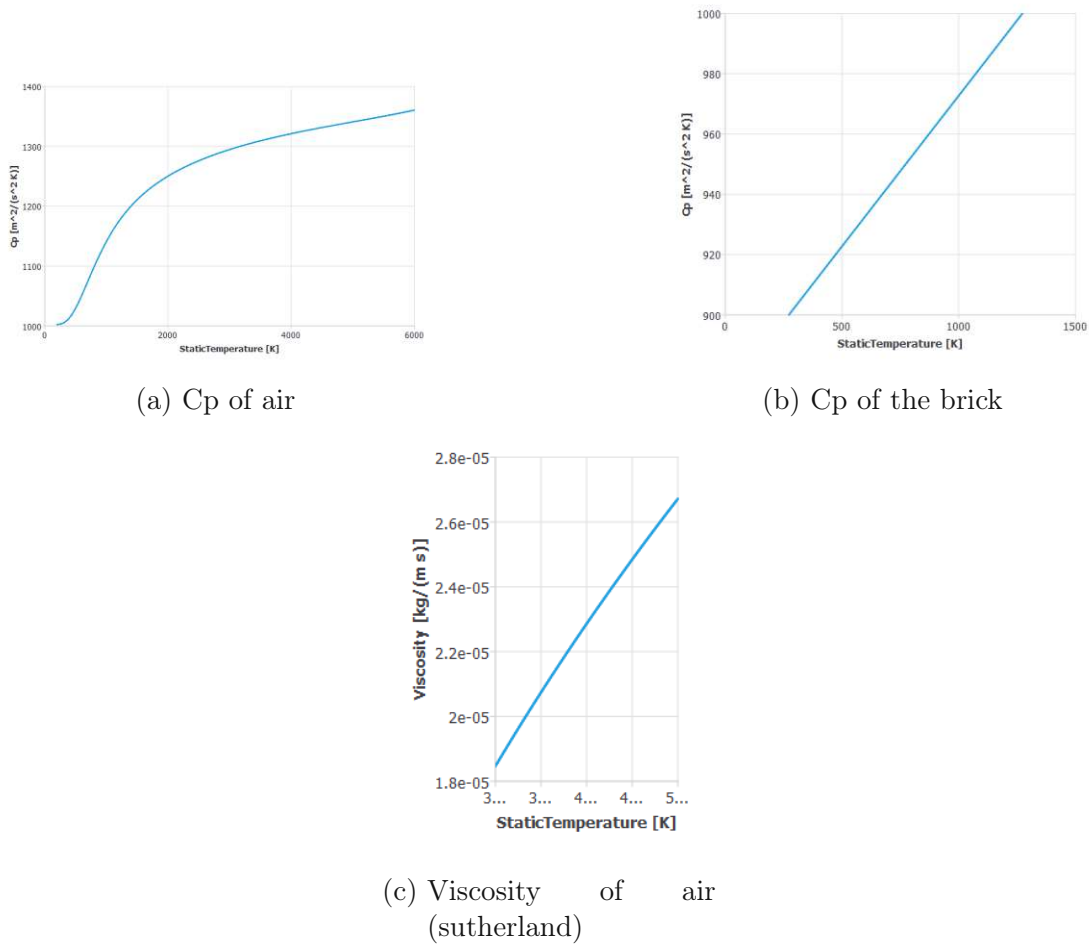


Figure 8: C_p of brick, c_p and ν of air.

3.2 Grid independence

In order to carry out a grid independence study, the small case with a mass flow of 0.4kg/s was used. Three different grids with significantly different cell numbers were created. As suggested by Celik et al. (2008) a refinement ratio of $r_g \geq 1.3$ was used. In order to prevent differences due to different y^+ values, the size of the first fluid cell was maintained constant through all refinements that lead to the same y^+ in all refinement levels. The method used is described in 2.5.2

because all simulations are transient the cases for the grid independence are also calculated transient but only until a time of $t = 2000s$ with a time step size of $\Delta t = 0.2s$. For the monitored quantities, three brick temperatures were chosen. The maximum brick temperature, minimum brick temperature and volume averaged brick temperature.

For the materials “brick” and “air” the properties listed in 3.1.3 were used in combination with the solution methods described in 3.1.1. The cell count of the three different grids and the refinement ratios are listed in Table(6). In Figure(10) the GCI calculated with Equation(21a) at every time step is plotted. Therefore, ϵ, p_c, q are evaluated at each time step. In Figure(10) the indices *min*, *max* and *avg* correspond to the minimum temperature, maximum temperature and the volume averaged brick temperature. One can see that there are several jumps that are caused by $\epsilon_{32}/\epsilon_{21} \approx 1$, which leads to very small values of p_c . Here $\epsilon_{32}/\epsilon_{21}$ is the ratio between the error between the coarse and the medium grid divided by the error between the medium and the fine grid. This can also be seen in Figure(11) where p approaches zero and corresponds every time to a high spike in the GCI. In Figure(12) the convergence ratio is in the range $0 \leq R_c \leq 1$ for the averaged temperature, which leads to monotonic convergence. For the maximum temperature, this is not the case. For the first ≈ 500 time steps there is $R_c \leq 0$, which leads to oscillating convergence. Also, another indication for oscillating convergence in this range is indicated by very small ϵ_{21} and ϵ_{32} values (Celik et al. (2008)). This is problematic, and the use of a least square version of the GCI should be considered (Roache (1994)). However, because the minimal temperature is not that important and is just considered here for completeness, the simulations with the least square version of the GCI has not been carried out. In contrast to the minimum temperature, there are some areas with monotonic convergence, some with

oscillating convergence and also some with divergence, which are characterized by $R_c > 1$. Furthermore, the values of ϕ_i/ϕ_i^{ext} for four different time points are plotted in Figure(9). Here it can be seen, that the error is growing over time for the volume averaged temperature, but monotonic convergence is maintained. For the maximum temperature at $t = 500s$ the oscillating convergence can be seen, but later this is not happening as seen in previous plots. The minimum temperature however starts out with oscillating convergence at $t = 500s$. Later it changes to monotonic convergence and at the end at $t = 2000s$ even divergence is observed, which leads to the error increase jump between $t = 1500s$ to $t = 2000s$. For all these temperatures, the differences between the fine(1) and the medium(2) grid are less than 1%, which is small enough to use the medium grid and not pay the costs of approximately twice as many cells. Also, this grid is duplicated five times for some simulations, and this would increase the cell count and therefore the simulation time even further. Hence, the medium(2) grid is used for the simulation or as a starting point for the complete mesh.

Table 6: Cell count and refinement ratio of grid independence study

cell count 1 (fine)	cell count 2 (medium)	cell count 3 (coarse)	r_{21}	r_{32}
865305	371280	147844	1.33	1.36

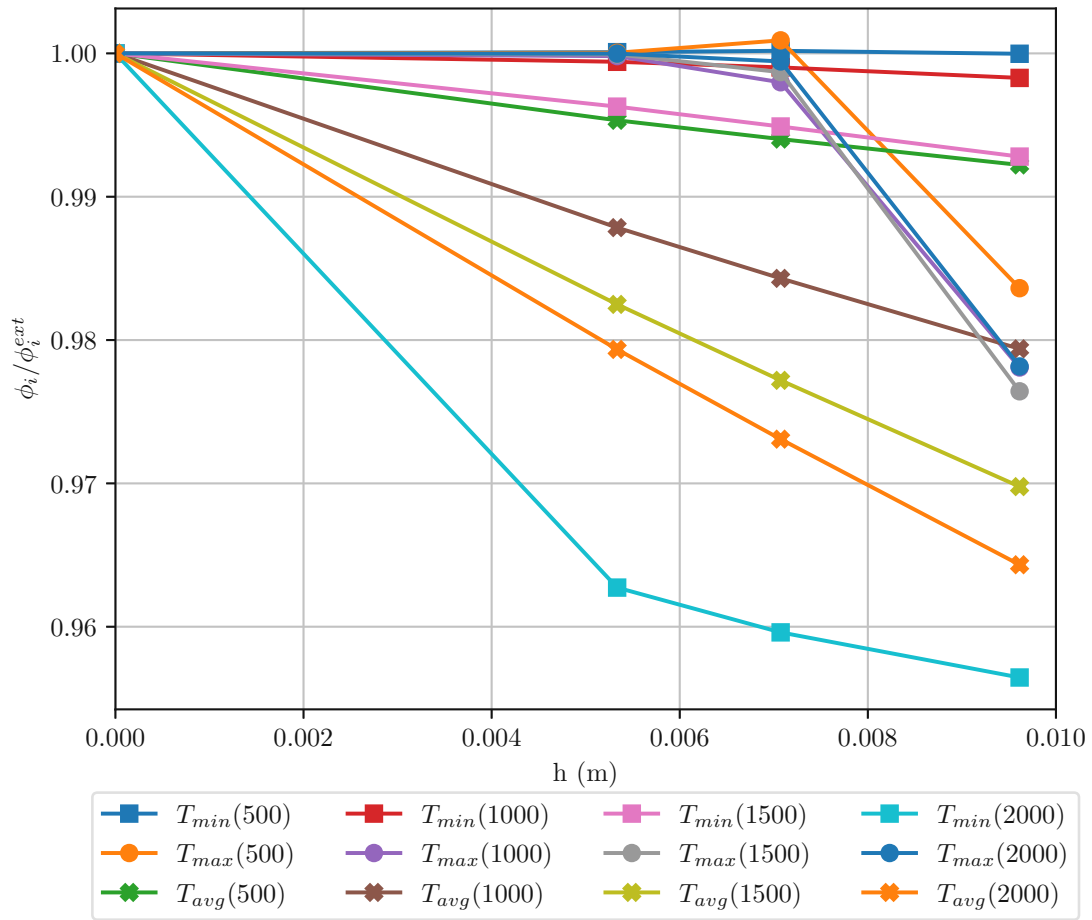


Figure 9: Plot of ϕ_i / ϕ_i^{ext} for the coarse, medium and fine grid.

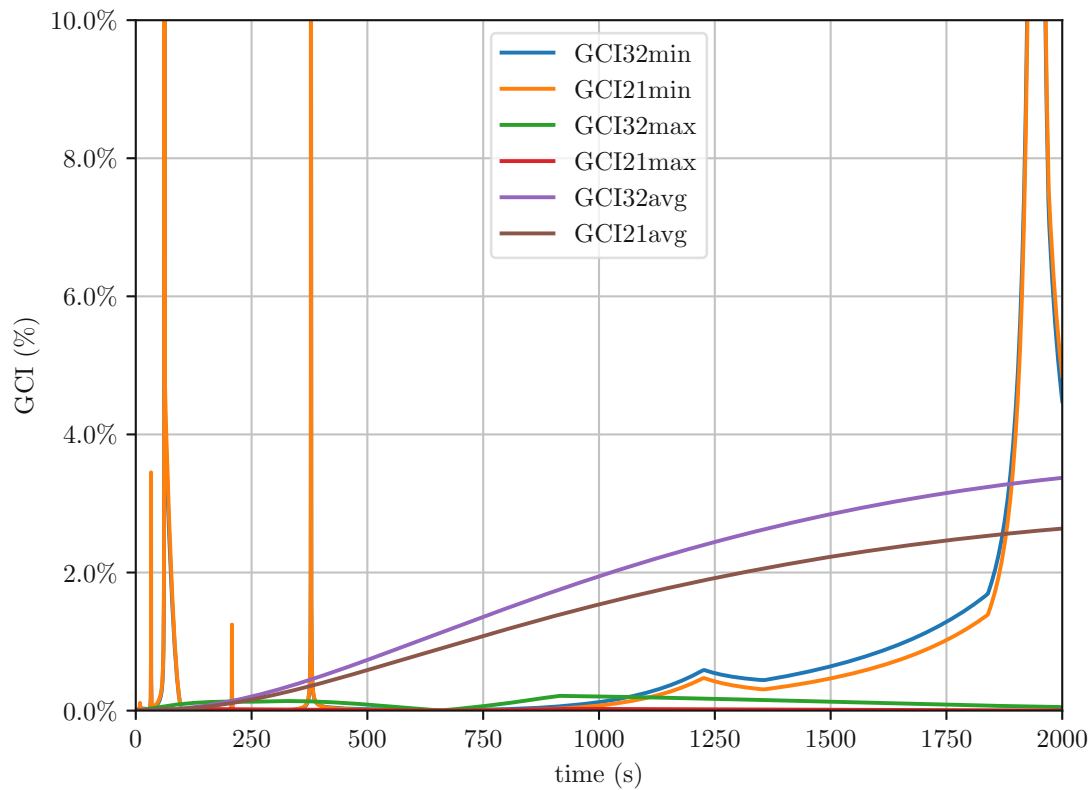


Figure 10: GCI over time.

3.3 Boundary conditions

In this section, the used boundary conditions for each case are described briefly. As there are many combinations the common boundary conditions, which are used in all configurations, are the listed (see Table7.). The symmetry was chosen to investigate a single brick positioned in the center of many bricks. The top and bottom wall represent the kiln car and the ceiling of the kiln and are assumed as adiabatic. This doesn't hold in reality, because although the kiln is insulated, there are significant heat losses over the length of the kiln. As the kiln cars can reach temperatures up to half of the brick firing temperature at the end of the firing zone,

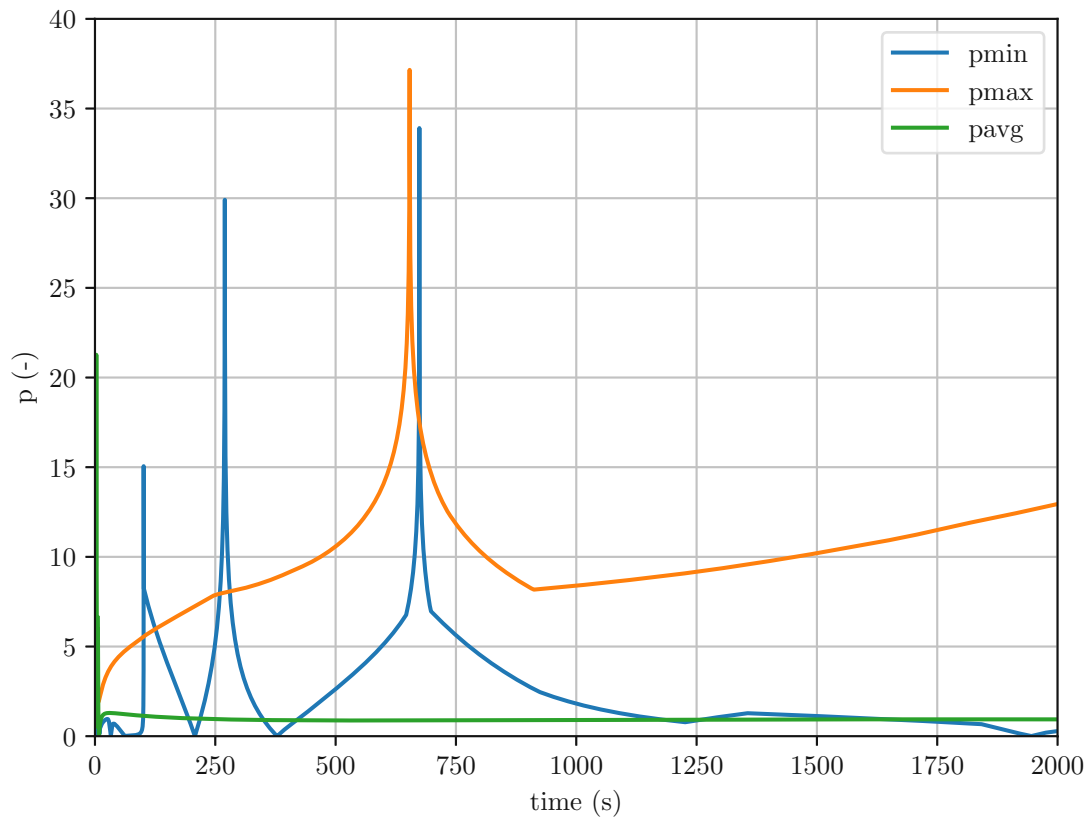


Figure 11: Plot of p calculated following Equation(19) over time.

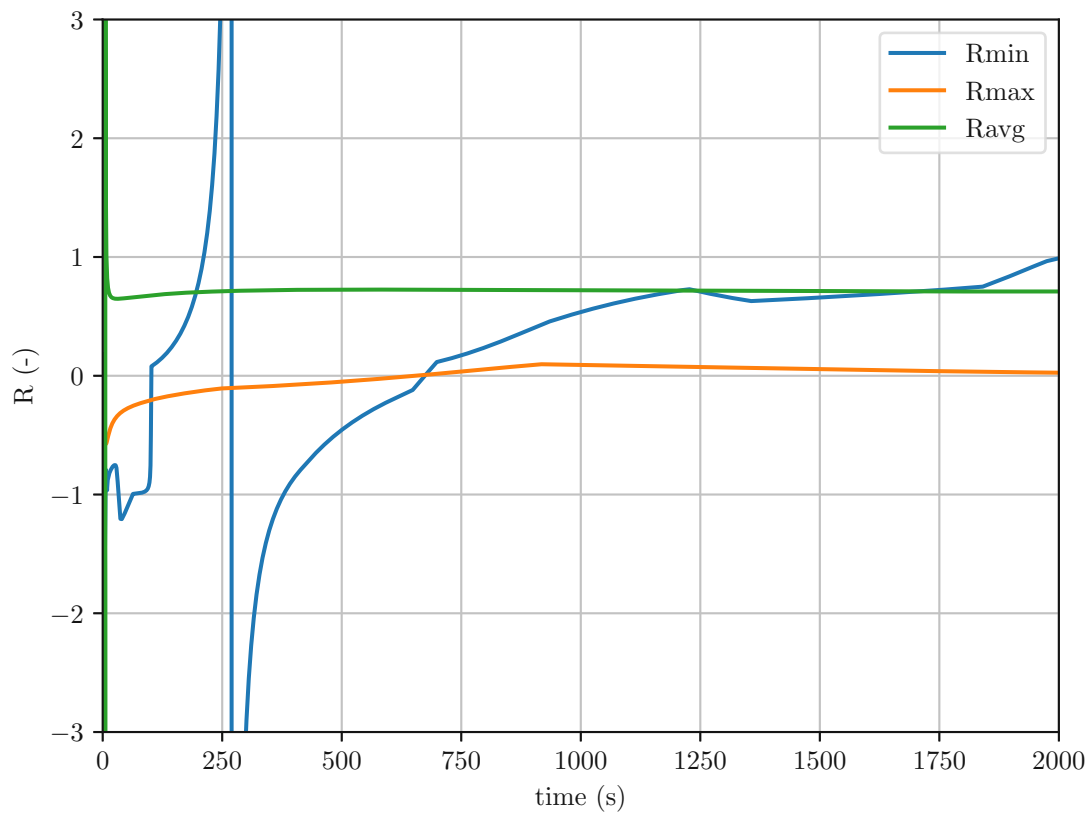


Figure 12: Plot of R over time.

an additional air volume is necessary in order to cool the cars. This is not visible in energy balances because there are only the relatively cool kiln cars at the entry or exit are accounted for. This ignores the storage and release of energy as the cars cycle through the kiln(Vogt (2017b)). Therefore, an easy further improvement would be to include the real ceiling with insulation and therefore the heat loss over the length of the kiln. This was not done here because of time shortage but could easily be implemented with the usage of a shell conduction model without any geometry changes. In order to use this model, one has to define the layer count as well as a thickness for each layer and a corresponding conductivity. In order to apply the correct boundary condition, the boundary condition is not applied on the wall surface anymore but instead at the last layer, as can be seen in Figure(13). This would also require changing the wall boundary condition from adiabatic to a fixed room temperature, which would then be applied to the last layer.

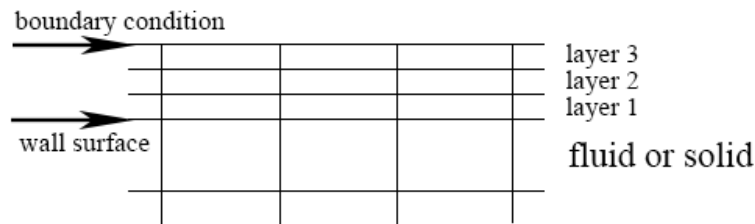


Figure 13: Shell conduction model with three layers.

In order to calculate the view factors necessary for the surface to surface radiation model only the top and bottom walls and the surface of the brick are included and have a temperature dependent emissivity defined as

$$\begin{cases} -0.0003T + 1.04 & T \leq 500K \\ -0.00024T + 0.992 & 500K \leq T \leq 700K \\ 0.68 & T > 700K \end{cases}$$

which can also be seen plotted in Figure(14). For the usage in fluent, this is modeled linearly because it's easy to implement and there was no experiment data for the temperature dependence of the emissivity available for the brick material.

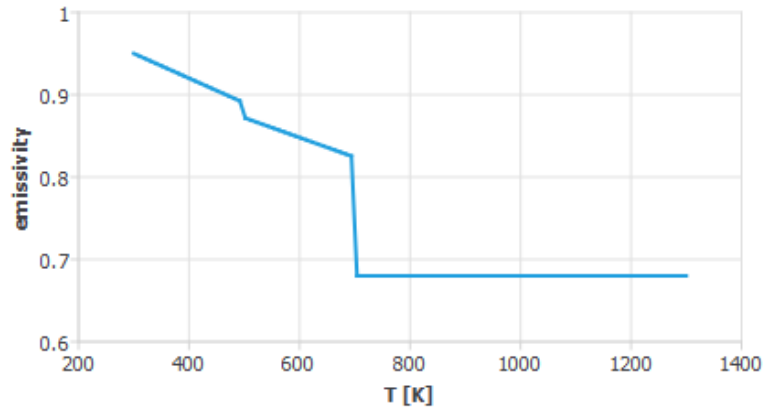


Figure 14: Emissivity of the brick material over temperature.

3.3.1 Temperature and velocity scaling

In order to simulate the heating of the brick the temperature of the inlet air is increased linearly from 30°C(303.15K) to 950°C(1223.15K), which leads to the linear function for the current time step

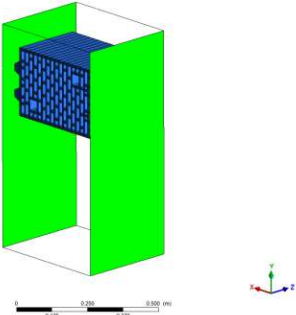
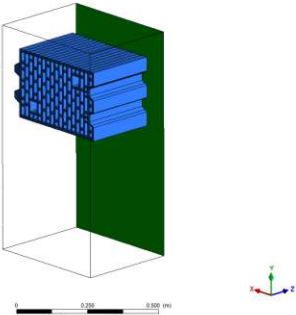
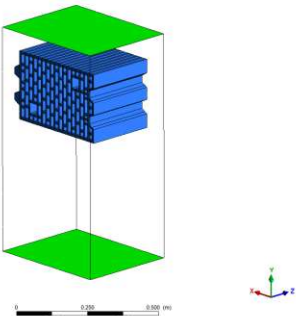
$$T(t) = 0.12778t + 303.15 \quad (27)$$

and

$$T(t + \Delta t) = 0.122778(t + \Delta t) + 303.15 \quad (28)$$

for the next time step, which is used for scaling the velocity profile. This temperature is set uniform on the inlet. In order to perform the transient simulation, first a velocity profile has to be obtained. Therefore, a setup with 5 bricks was

Table 7: Common position and type of used boundary conditions used in all cases

position	type
	<p>symmetry</p>
	<p>pressure outlet</p>
	<p>wall</p>

3 Numerical Setup & Methodology

used (see Figure15) and a steady state simulation was performed. For the first approach cases, the steady simulation was performed on the same mesh with one brick. Then the velocity in each direction, the turbulent kinetic energy and the specific dissipation rate were saved at the marked position Figure(15) and scaled like the following

$$v_z(t + \Delta t) = \frac{v_z(t)T(t + \Delta t)}{303.15} \quad (29)$$

. This scaled velocity is set component wise on the velocity inlet, where only the stream wise direction(z-direction) is scaled accordingly.

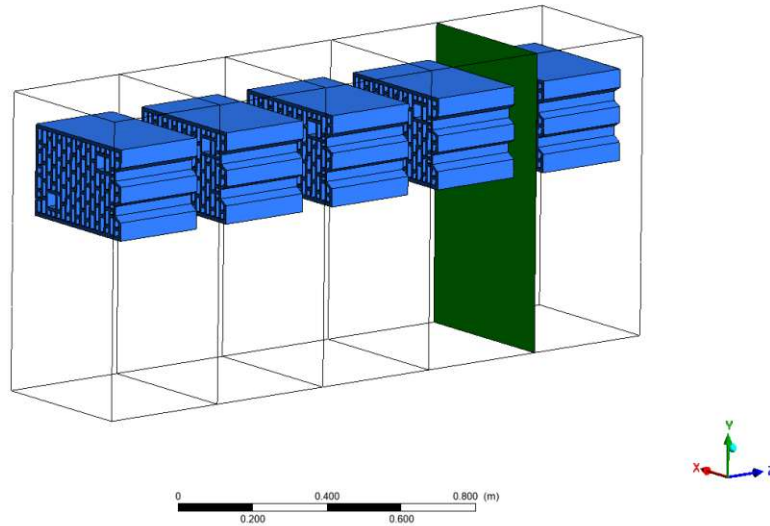


Figure 15: Plane at which the profile is taken

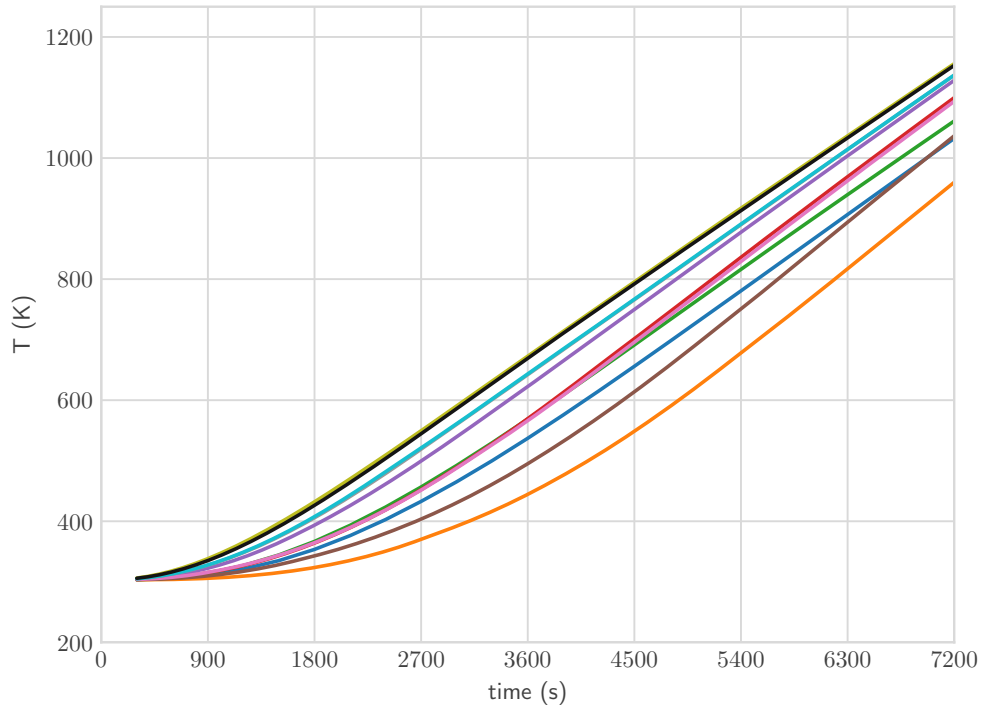
Table 8: Mesh metrics.

Number of elements	large	small	offset
Max aspect Ratio	9.22	6.52	11.51
Min aspect Ratio	1.07	1.05	1.02
Min determinant	0.22	0.19	0.19
Max Skewness	0.86	0.86	0.9
y_{max}^+	15.83	19.5	24.6

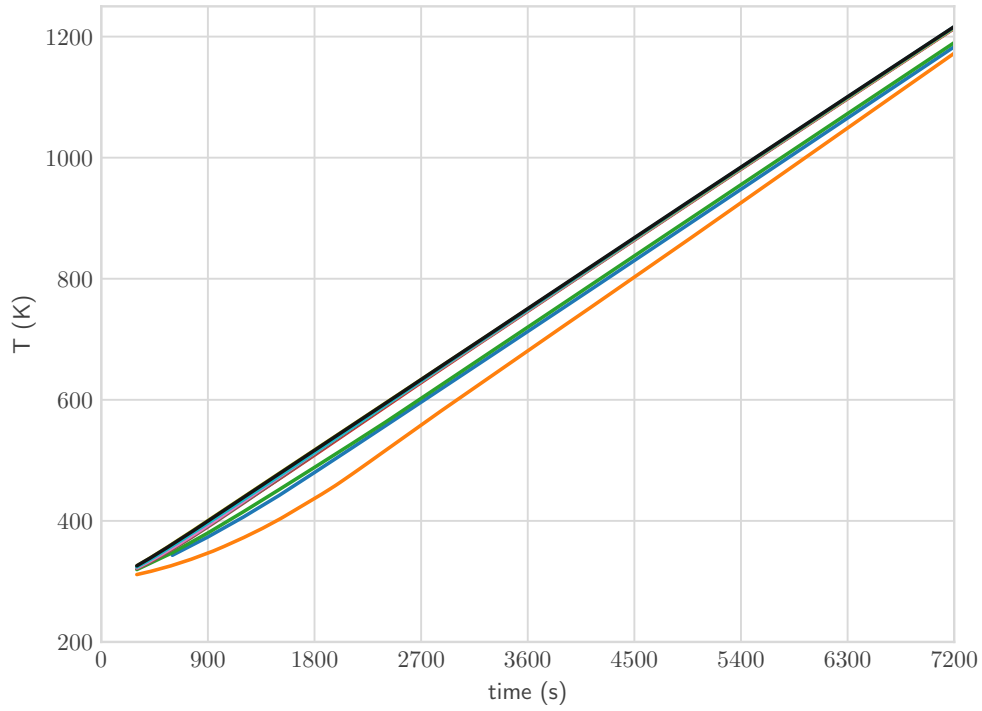
4 Results & Discussion

The first simulations carried out were the cases *small first approach* and *large first approach* (see Table(1)). In these simulations, the velocity profile used for scaling was obtained by a steady simulation on the same mesh. Both cases were simulated for two different mass flows of $0.4kg/s$ and $0.6kg/s$ but the mass flow of the small case was scaled by the inlet area according to $\dot{m} = \frac{A_{small}}{A_{large}}$. The scaling of the mass flow lead to different values of $0.3kg/s$ and $0.45kg/s$ for the small case, but for simplicity they are referenced as 0.4 or 0.6 accordingly. The described setup lead to following temperatures in the brick and effective alpha values Figure(16) with the definition for the effective alpha Equation(22a). There is a noticeable difference between all small and large cases, as for the small cases the calculated effective alpha is a bit higher than for the large cases. Also, a larger mass flow increases the effective alpha, as expected because a higher mass flow leads to higher velocities. In case of the offset bricks, the effective heat transfer coefficient is about the same as for the small case, which indicates that the same heat transfer could also be accomplished with better positioning of the bricks on the kiln. The problem arises as of which quantities should be taken into account in order to compare different cases. For the first approach, only the minimal, maximal, and volume average temperatures and the effective alpha were considered. Later also histograms of temperature distribution in the brick

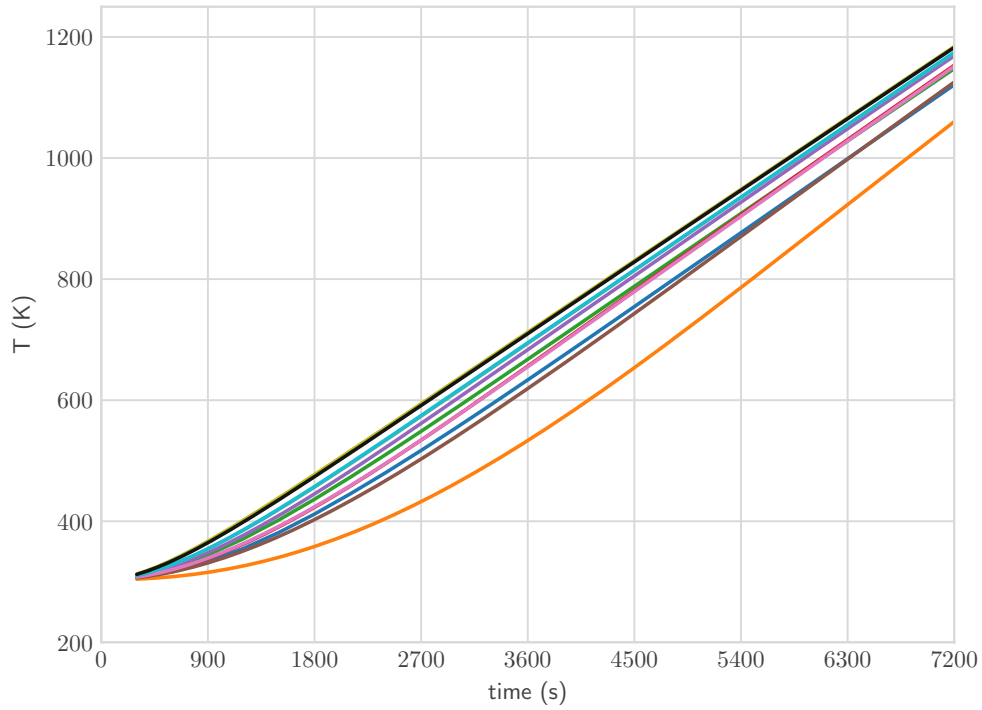
were taken into account. In order to create the histogram of temperature over percent of volume, the temperature range between 775 °C and 950 °C was split into intervals. Then the cell volumes with the corresponding temperatures were exported, and the volumes summed up to the nearest temperature interval. At last, the cell volume in each interval was divided by the total volume to get the percent representation.



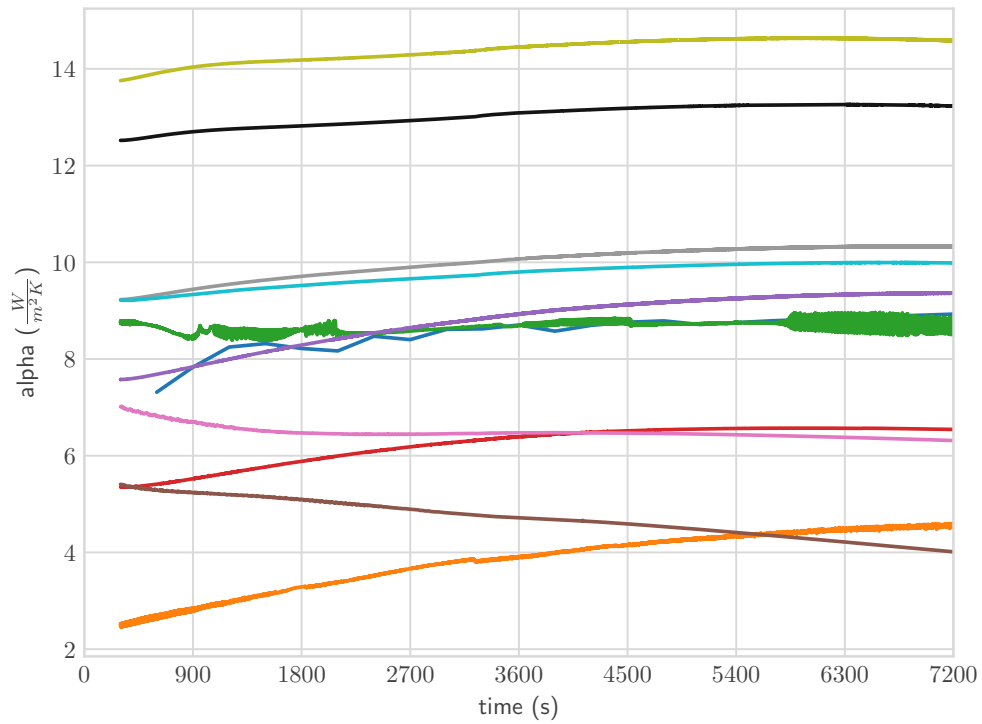
(a) Minimal temperature in the brick.



(b) Maximal temperature in the brick.

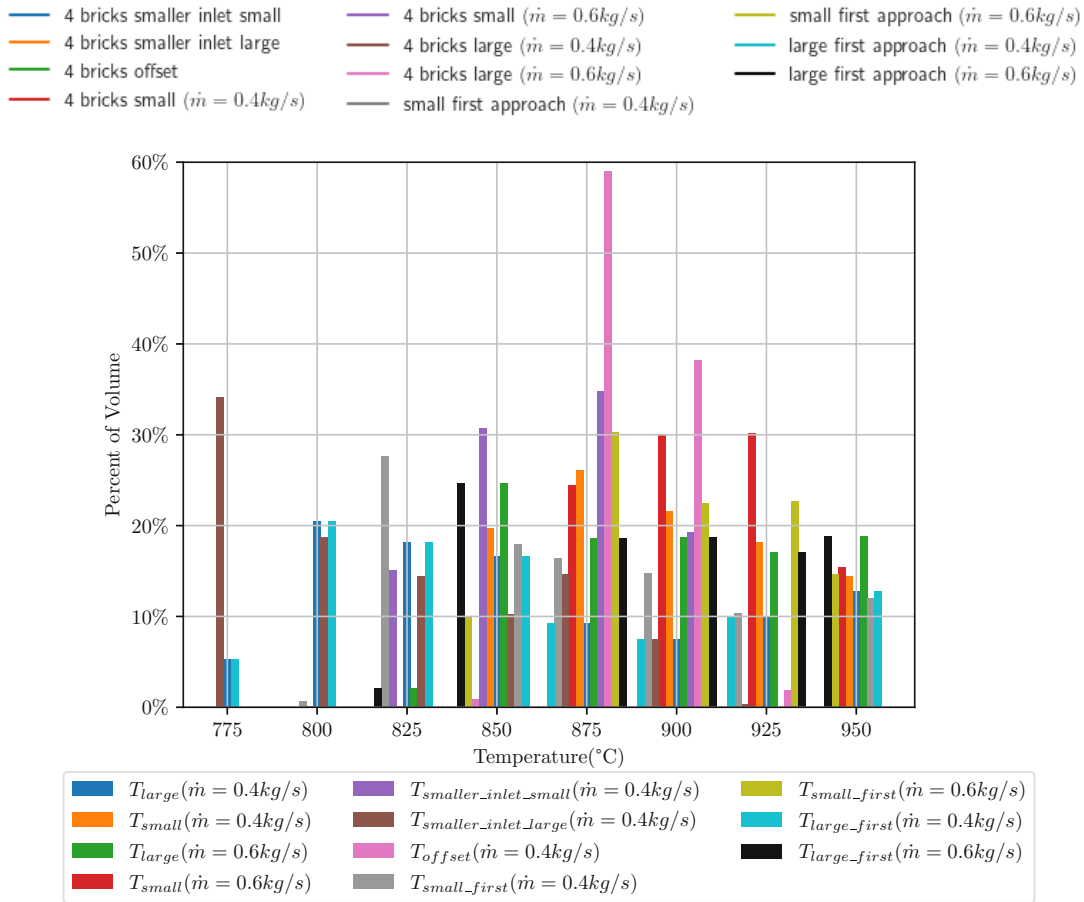


(c) Volume averaged temperature in the brick.



(d) Effective alpha in the brick.

4 Results & Discussion



(e) Temperature distribution in brick.

Figure 16: Temperature, effective alpha, temperature distribution and total heat flux.

There can be seen that the average temperature differences between the small and the large case are $< 1K$ for the first approach cases, $< 30K$ for the 4 brick cases and $< 60K$ for the smaller inlet cases. The average temperature for the small cases was always higher than for the large cases. Notably the minimum- and the average brick temperatures of the *4 bricks offset* is higher than at the *4 bricks smaller inlet small* case which indicates a more uniform heating. This can also be seen in the histogram of temperature distribution. Also, the temperature

Table 9: Difference compared to the offset case.

	large	small
$\Delta T_{min}(K)$	-101.3	-28.8
$\Delta T_{max}(K)$	-17.5	-6.8
$\Delta T_{avg}(K)$	-26.6	-87.4
$\Delta t(s)$	-600.0	-300.0
$\Delta \alpha_{eff}(\%)$	-49	1

distribution of the small cases trends towards higher temperatures and therefore can grant a more uniform heating of the brick, which could lead to better quality. For the effective alpha the highest values were achieved with the *first approach* cases, however these setups were calculated with a constant mass flow at the inlet which led to a completely different velocity profile than in the other cases. Furthermore, the cases with higher mass flow lead to higher velocities and therefore to higher effective alpha values. For the *4 bricks offset* case the effective alpha is only one percent smaller as for the *4 bricks smaller inlet small* case which shows that the arrangement of the bricks makes a big difference as also stated in (Vogt (2017b)). The effective alpha difference between the *4 bricks offset* and the *4 bricks smaller inlet large* was about 49%. After the first simulations with the scaled velocity profile, The conclusion was that maybe the velocity profile at the out-plane may look different after the next brick. Therefore, a large error is made due to a varying velocity profile. After creating a new mesh with 4 bricks and investigating the velocity profiles Figure(17) one can easily see that the profile changes significantly from right to left. The first profile on the left is after the fifth brick near the outlet, and due to influences near the outlet the profile after four bricks was used for further simulations.

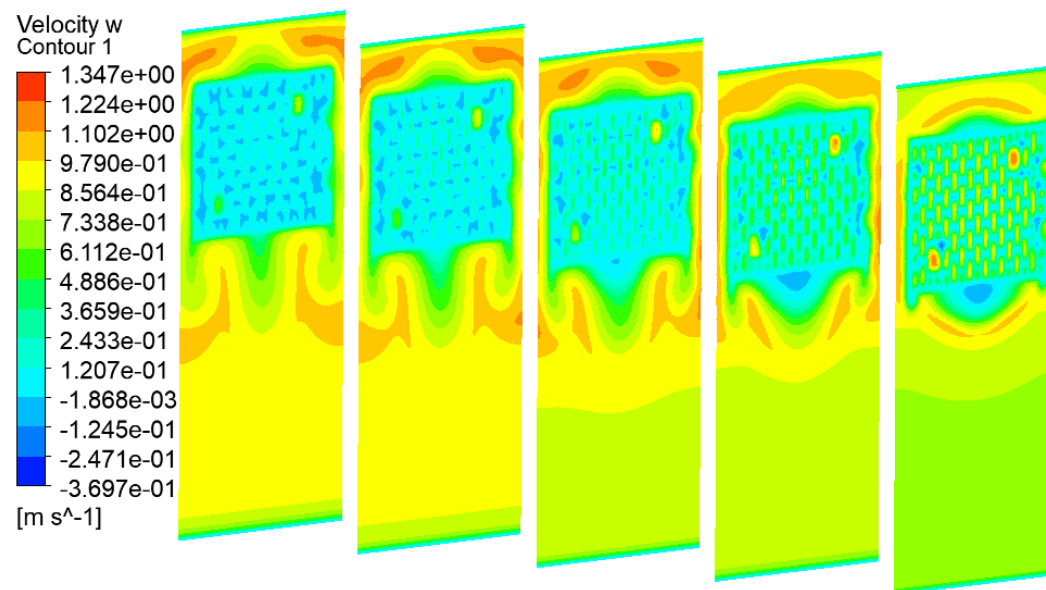


Figure 17: Stream wise velocity profile after each brick.

As observed, only a small percentage of the mass flow \dot{m} passes through the brick and the majority around the brick. Because the area of the holes in the brick are around 80% of the total area, the heat transfer would be improved if more air passes through the brick and not around the brick. However, for the *4 bricks offset* case, the amount of air passing through the brick increases compared to the *4 bricks smaller inlet large*. Offsetting the bricks led to an even larger improvement than just lowering the ceiling. This can also be observed in the velocity contour plotted in Figure(20). In Table(10) the percentage of the mass flow passing through the brick is plotted for the third and fourth brick. There can be seen that for the *4 bricks smaller inlet small* and *4 bricks smaller inlet large* cases, the least mass flow through the brick happens at the third brick. This can also be noticed in the large case in Figure(21) where the air inside the third brick is much colder than in the others.

Table 10: Percentage of the total mass flow passing through the brick

case	mass flow through brick(%)
4 bricks offset(3 rd brick)	13.6
4 bricks offset(4 th brick)	13.6
4 bricks smaller inlet small(3 rd brick)	9.0
4 bricks smaller inlet small(4 th brick)	12.0
4 bricks smaller inlet large(3 rd brick)	2.2
4 bricks smaller inlet large(4 th brick)	3.3

In order to see the conditions inside one hole, the Reynolds number with the hydraulic diameter of one hole was formed. Furthermore, the velocity \vec{u} and temperatures were extracted along three vertical lines, which can be seen in Figure(18). This was done to clarify if relaminarisation takes place inside the hole after the entrance.

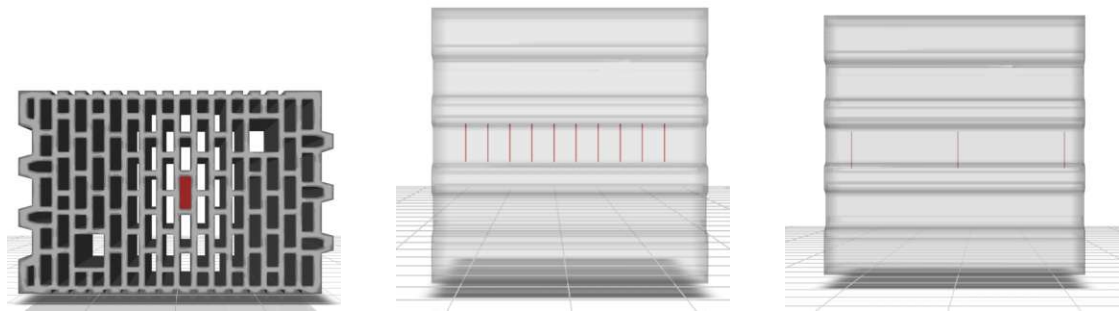
In Figure(18) one can see that the maximal Reynolds number is about 525 which is completely in the laminar flow regime. This led to the conclusion that there is no transition happening. Furthermore, the velocities in the holes will be even lower, because of the smeared holes from cutting the brick (see Figure(19)). In the next approach, the inlet velocity profile was obtained at a separate simulation with five bricks,



Figure 19: Picture of the cut brick.

described in Section 3.3.1. The resulting velocity profile obtained is plotted in Figure(22a) and can be seen to differ quite strong compared to the first approach profiles. Also, the scaling of the mass flow with the area was omitted and a mass flow of 0.4kg/s and 0.6kg/s was used for the small case.

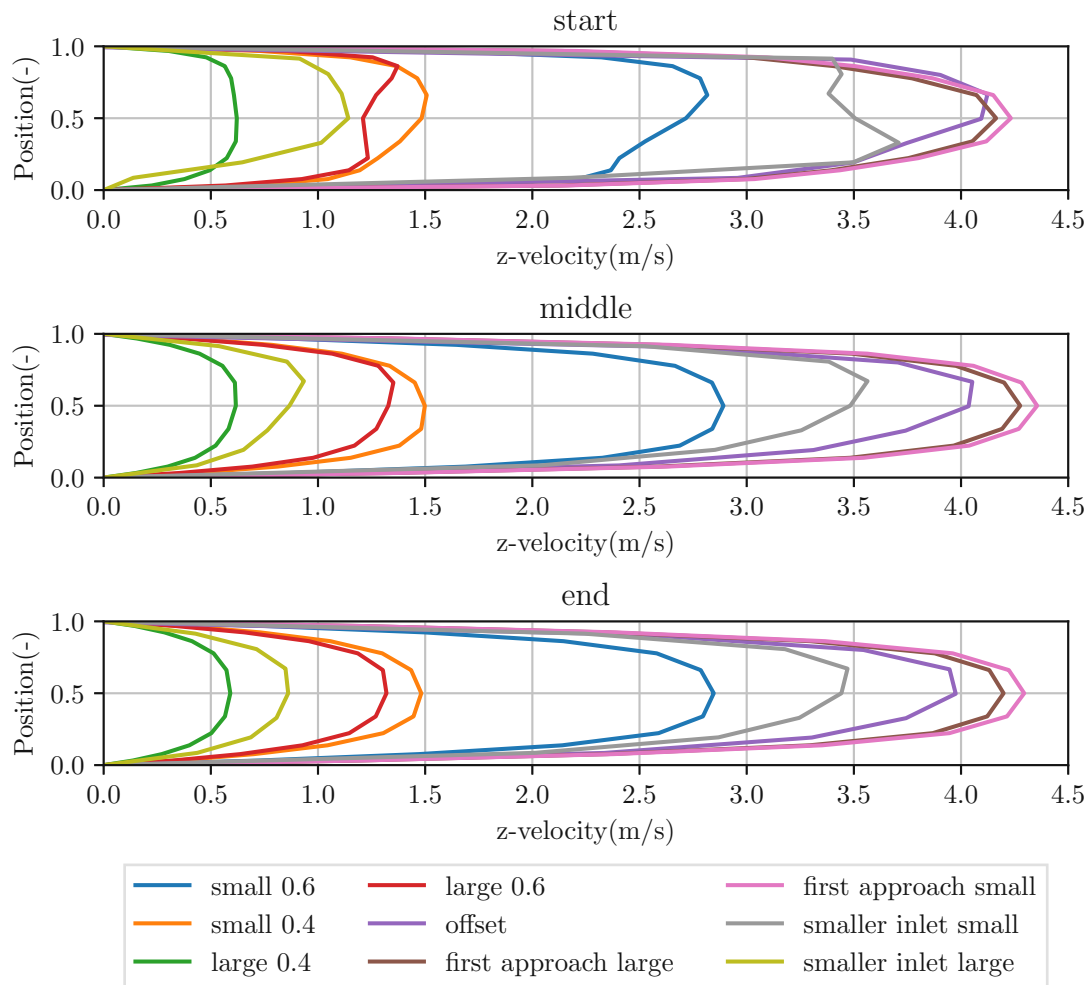
After a revisit of the kiln car, a more precise model of the brick including the



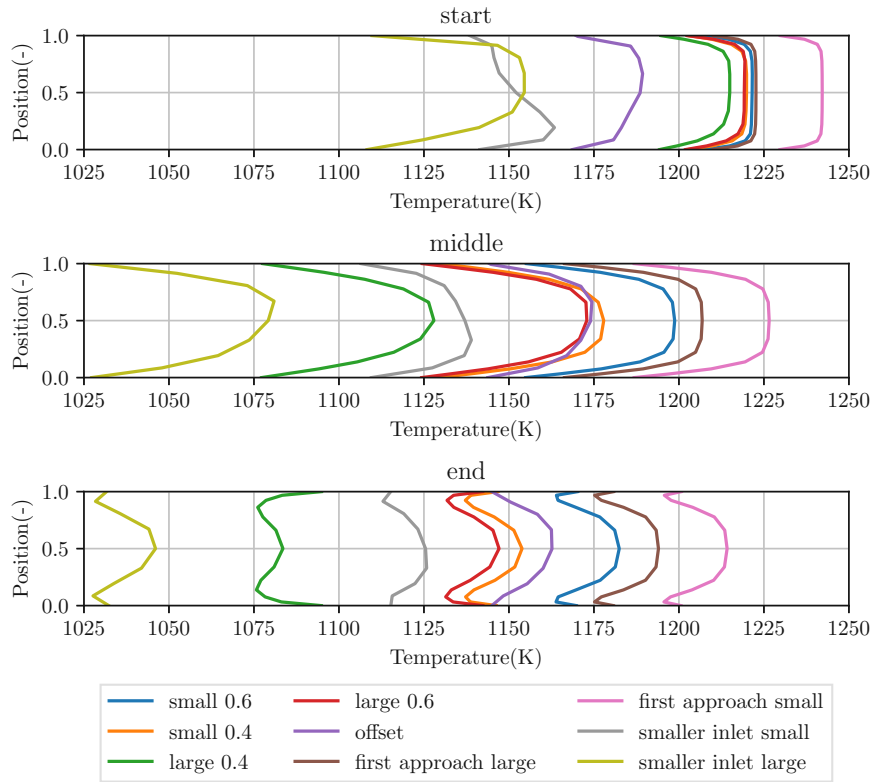
(a) Position of the investigated hole.

(b) Positions of the planes in the hole.

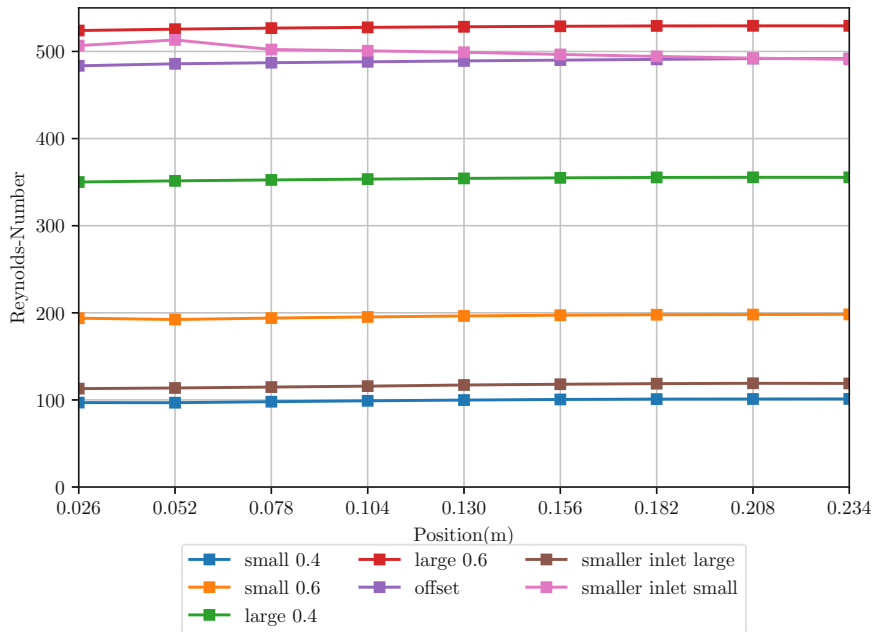
(c) Position of the lines inside the hole.



(d) Velocity at lines in the hole.



(e) Temperature at lines in the hole.



(f) Reynolds number at the plane.

Figure 18: Positions in the hole, velocity and temperature along line.

support and the flow barrier was created in order to get a more realistic model. This new model contains four bricks in a row and removes the necessity of a second model for a steady state simulation to obtain the velocity profile. Furthermore, two different models with different heights were created, refereed as small and large according to Table(1). The same mesh was used for the steady simulation to get the velocity profile and the transient setup. For the cases *4 brick smaller inlet small* and *4 brick smaller inlet large* the setup above was used.

In the last simulation, an alternative to lowering the ceiling in the kiln was provided by offsetting the bricks. In order to achieve this offset, the supports of the bricks on the kiln cars has to be alternating lowered or raised. This is also much simpler and cheaper than lowering the ceiling inside the kiln.

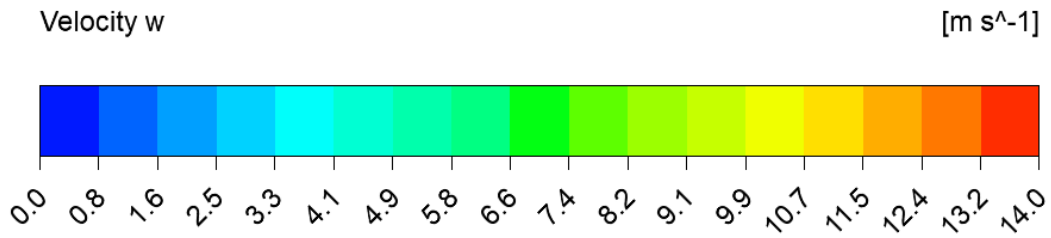
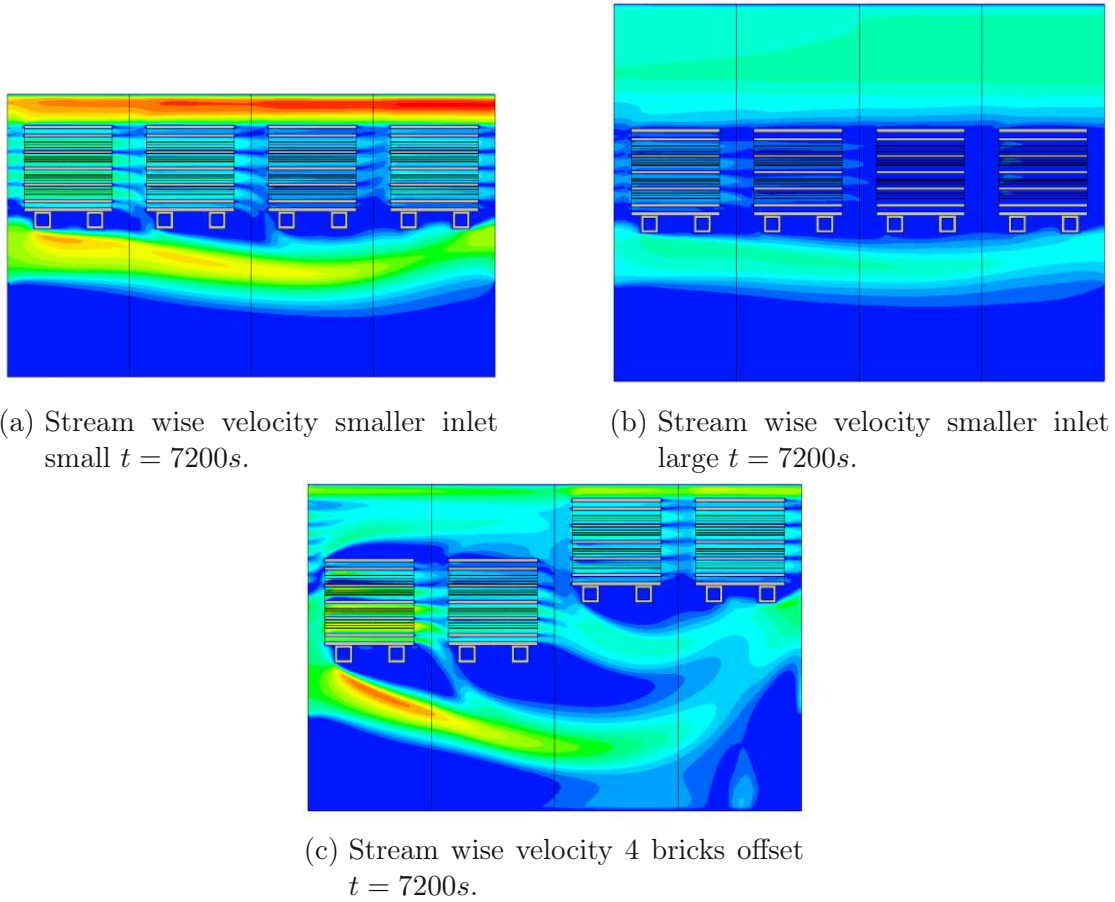


Figure 20: Contour of the stream wise velocity at the end of the simulation.

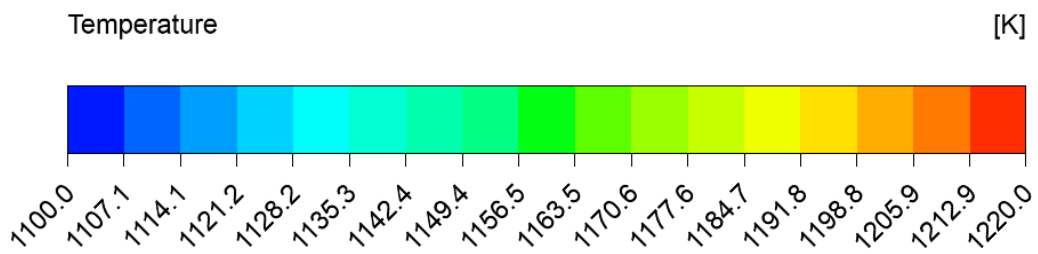
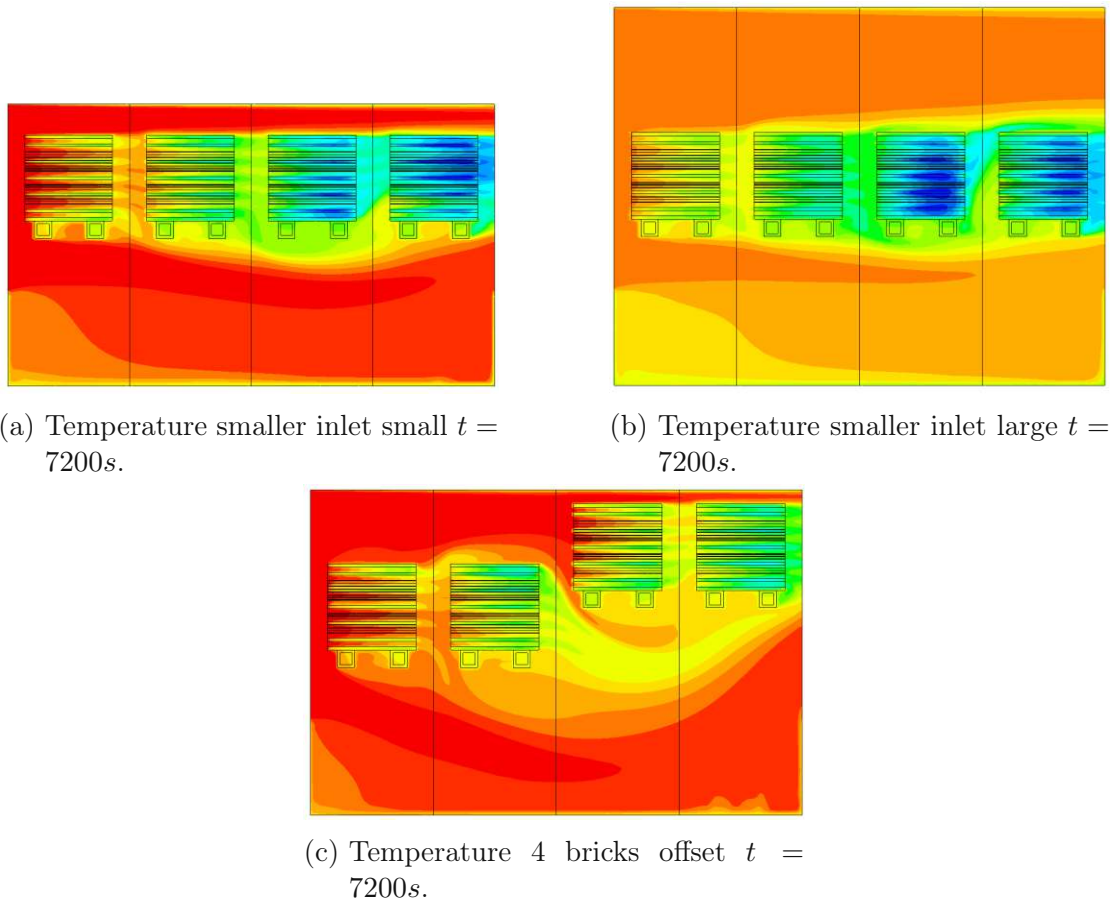
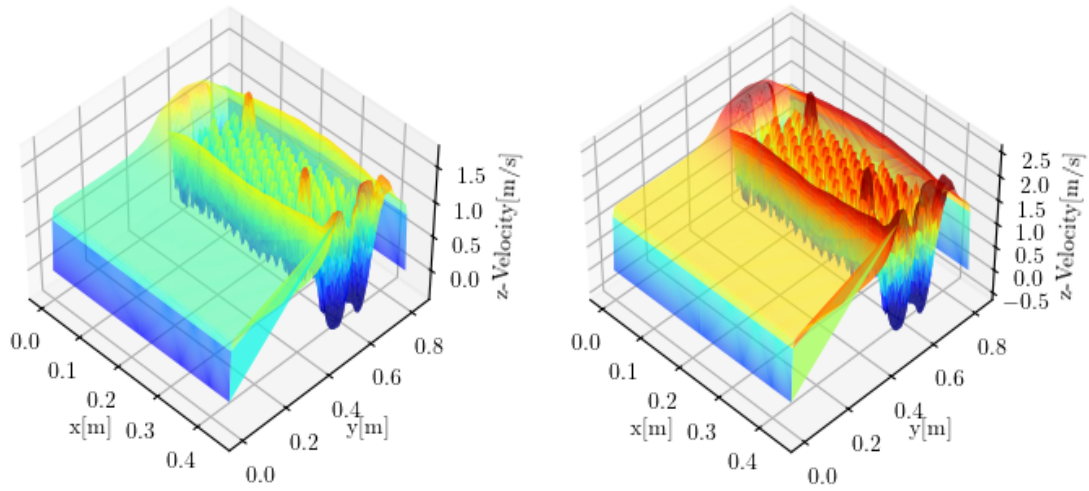
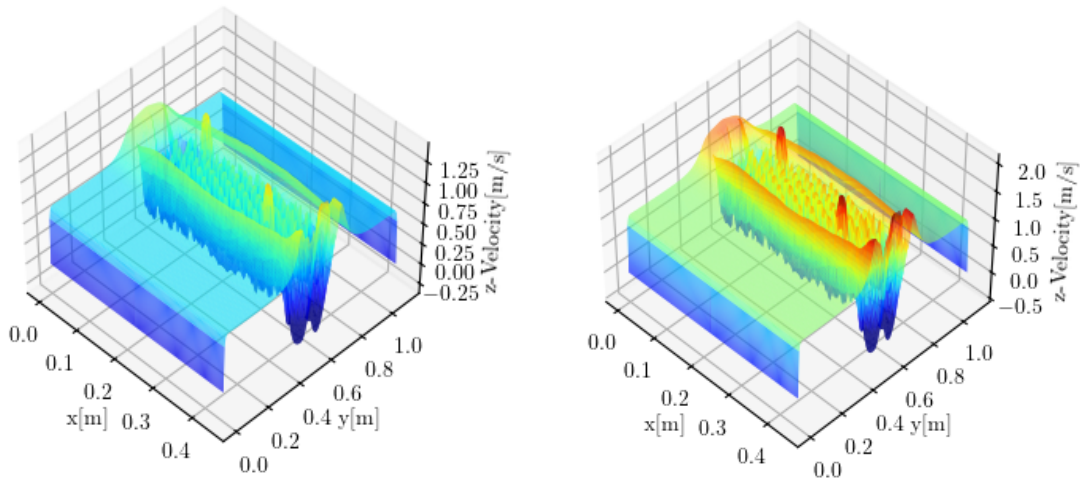


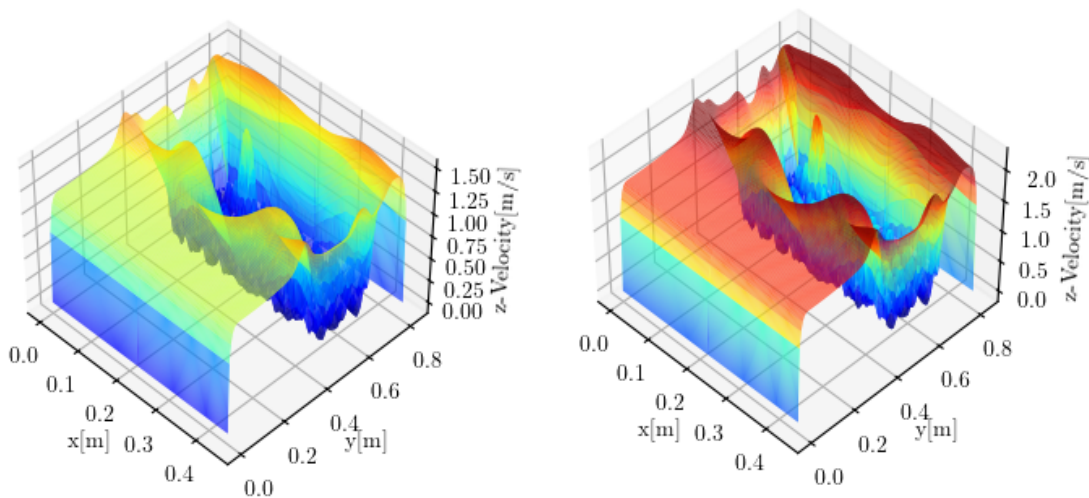
Figure 21: Contour of the temperature at the end of the simulation



(a) Velocity profile small first approach 0.4. (b) Velocity profile small first approach 0.6.



(c) Velocity profile large first approach 0.4. (d) Velocity profile large first approach 0.6.



(e) Velocity profile 4 bricks small 0.4. (f) Velocity profile 4 bricks small 0.6.

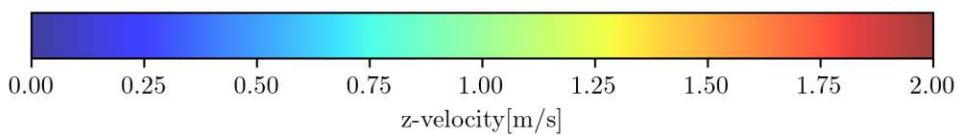
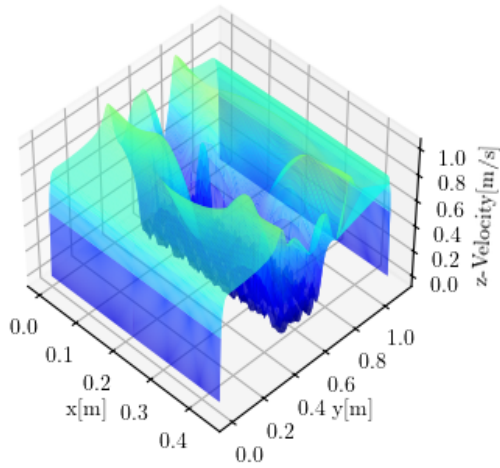


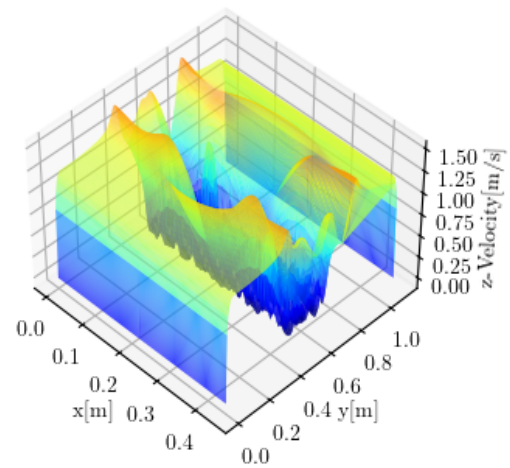
Figure 22: Velocity profiles

4.1 Pressure Drop

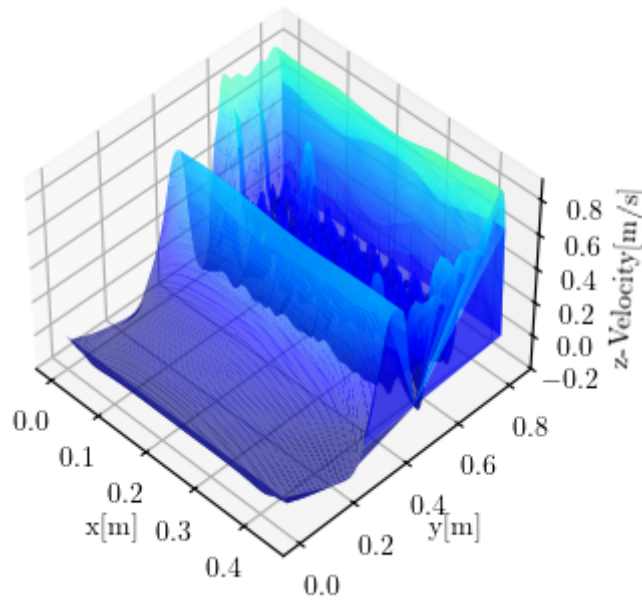
The pressure drop is an important parameter in order to maximize the specific heat transfer coefficient but is also limited by the power requirement of the fans to reach these pressure drops along the kiln. As stated in Vogt (2017b) the maximum reasonable pressure drop along the kiln is about $200Pa/m$ which results in a total pressure drop of about $8000Pa$ over the total length of the kiln. This is considered the maximal reasonable pressure drop, which leads to a much bigger heat transfer coefficient and therefore shorter firing time. As can be seen in Table(11). There is no firing time specified for the simulated cases because only the heating is simulated, and the firing time would also include the cooling of the bricks. In order to reach these high pressure drops, much more powerful fans are required than those commonly in use. There are many kinds of bricks, for example backing bricks, facing bricks or roof tiles. As not all of them are directly onto the kilns, some are placed inside stack able supports and then placed onto the kiln cars. This would result in a large variance of geometries which are placed inside the kiln, and therefore only backing bricks are considered here. These backing bricks have a large free internal cross-section and need much higher velocities inside the kiln in order to reach fast firing times. These high velocities are not reachable with an air to product ratio of 1 which should not be pursued according to the theory of heat exchange. Here, the air to product ratio is the relationship between the mass flows of gas and mass flow of bricks through the firing channel. Therefore, a larger mass flow of air is required to reach reasonable convective heat transfer and firing times. In order to get high pressure drops along the kiln, there are two main parameters which can be optimized. The first is the usage of fans which are able to deliver higher pressure than the currently used ones. The second is the placement of the bricks on the kiln cars. The gaps between them as well as the edge gaps should



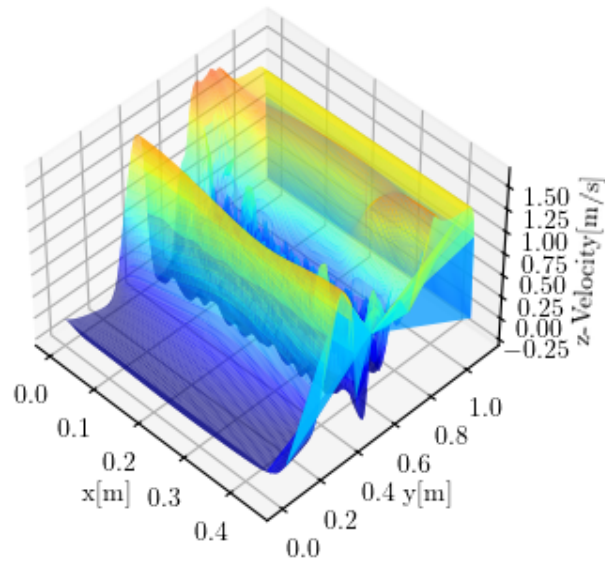
(g) Velocity profile 4 bricks large 0.4.



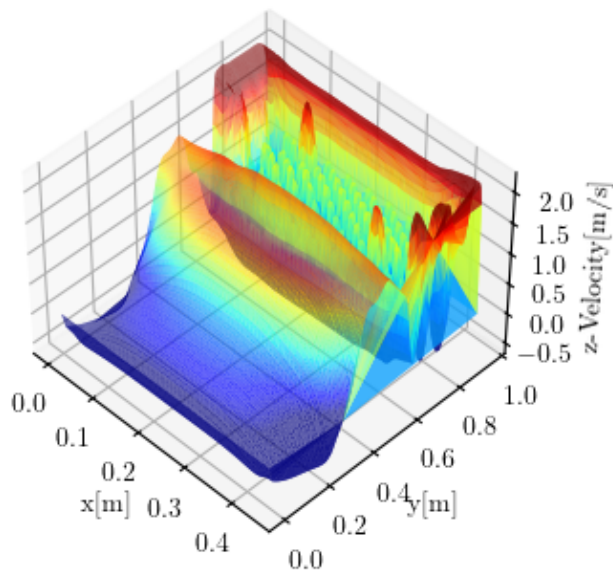
(h) Velocity profile 4 bricks large 0.6.



(i) Velocity profile smaller inlet small 0.4.



(j) Velocity profile smaller inlet large 0.4.



(k) Velocity profile smaller inlet offset 0.4.

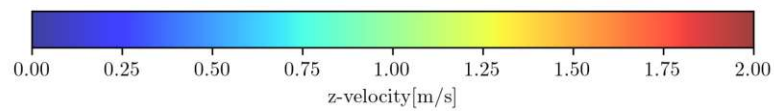


Figure 22: Velocity profiles.

be as small as possible Vogt (2017b). However, in the considered cases the mass flow of air was limited to a maximum of, 0.6kg/s which also limits the reachable velocities inside the kiln. Also, the placement of the bricks on the cars was fixed and could not be altered. As stated in (Vogt (2018)) the over all electric energy consumption is low compared to the consumption of thermal energy. Therefore, it can be useful to improve the heat transfer process by consuming more electric energy for stronger fans.

Table 11: Comparison of pressure drop and heat transfer coefficient

Firing time (h)	heat transfer coefficient (W/m^2K)	Pressure drop (Pa/m)	case
14.5	15.2	5.4	
6.7	30	54.0	
3.2	64	200.0	
-	9.0	9.9	offset
-	8.9	13.6	smaller inlet small
-	4.6	0.3	smaller inlet large

4.2 Validation

In order to validate the results of the simulation setup a series of measured air and brick temperatures were provided. These series containing temperatures from the whole way through the kiln starting from room temperature heating up to a maximum temperature and cooling down again to room temperature. In order to compare these provided brick temperatures with the results of the simulation, the case setup *validation* in 1 was used. In order to improve the physical simulation even more, the temperature profile after the fourth brick was saved, scaled and mapped to the inlet. After further investigation of the temperature profile during the simulation time, the investigated profile downstream of the bricks differs quite strongly from the uniform block profile used at the inlet in all other cases. It was

also considered to map the scaled temperature profile onto the inlet at all other cases but was not done due to unreasonable calculation time increase. But for the *validation* case, the step of mapping the scaled temperature profile onto the inlet as well as the scaled velocity profile was taken. The way this was handled was by writing a temperature profile with the fluent write profile utility, reading the profile again and scale it by a factor. As this involves writing to disc which is compared to in memory operations relatively slow, the implementation of a UDF (User defined function) which does this mapping would have been beneficial. However, as writing UDFs in Fluent especially for the multithreaded case is not straight forward, needs a lot of testing and debugging and time was limited this route was not taken. In contrast to all other cases, the inlet temperature was not increased linearly, but instead the measured series of air temperatures was used as inlet condition. Also, after reaching the maximum temperature, the mass flow for the cooling side was increased up to 1kg/s . All temperatures were evaluated at the fourth brick. As there was no information provided at which point the temperatures were measured but only the position of the brick on the kiln. Therefore, twelve points were considered and plotted as bands in Figure(23). These points are also visible in the small inset Figure(23). There were three points equally spread along the middle of the brick, and then two different depths from the front and back side were considered. These measurement points were placed as shown in Figure(23) at two different depths from both ends of the brick. Here, all simulated brick temperatures are below the measured values in the case of heating. There are two areas where the measured brick temperatures change the gradient, at 573°C and 870°C which correspond to changes in the crystal system of the brick material. These slope changes can not occur in the simulated temperatures, as these effects were neglected. For the cooling part, much better agreement with the measured data can be observed.

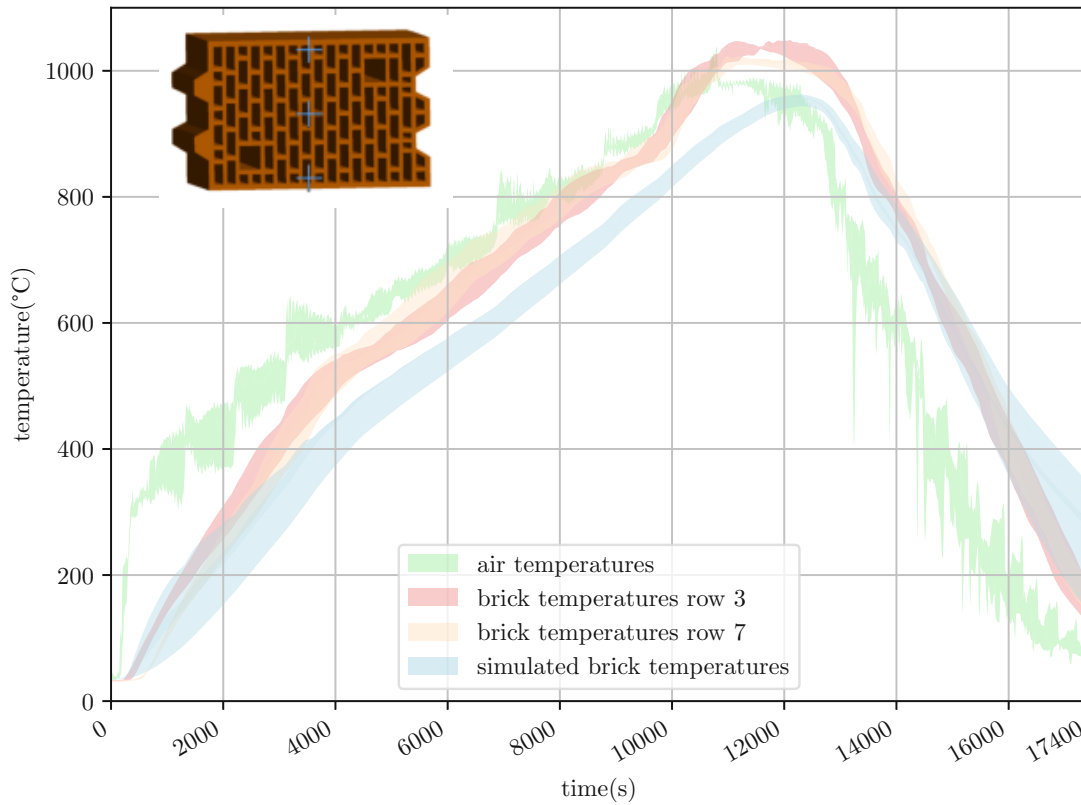


Figure 23: Comparison of measured brick temperatures and our simulated brick temperatures at the best fitting measurement point.

5 Conclusion & Future Research

In order to optimize the overall heat transfer of a brick inside a kiln, there are many parameters to consider. With the finally received model, there would be far more opportunities to simulate than it was possible in reasonable time. There are areas which were not considered as not that important but turned out to be crucial. One of these areas is the placement of the bricks on the kiln cars, which has a major impact on the heat transfer even without lowering the ceiling. Overall, the idea of a very complicated and expensive lowering of the kiln ceiling does not bring enough of the desired increased heat transfer and therefore lower firing time. There are other areas of these kilns which are easier to optimize and bring bigger advantage. Additionally, the ceiling and the kiln cars should not be modeled as adiabatic but instead in closer approximation to reality with different layers of insulation material. As the placement of the bricks is crucial, there are many possibilities to try different patterns of alternating lowered and raised bricks or even offset rows in between combined with lower gaps on the side and the top. There are many possibilities that are only limited by the maximum allowed pressure drop along the kiln. These considerations are way beyond the scope of this work but could definitely be investigated in further work. In order to get the maximum out of a kiln, every aspect has to be optimal, which is not easy to achieve as kilns are quite big in scale and very small changes can lead to a big difference. The main points of optimizations are

- insulation and sealing
- kiln cars and positioning of bricks
- pressure drop along the kiln

5 Conclusion & Future Research

as well as other factors like the geometry of the kiln which can not be altered easily. But many of the currently used kilns are quite old and would require immense investment to bring them to a current technical standard, which is often not worth it. Here, the solutions can perfectly assist the planning of next generation kilns.

List of Figures

1	Principals of a fast firing brick kiln.	3
2	Sankey diagram of mean energy balance[Vogt (2017b)]	5
3	radiant interchange between tow area elements[Venkateshan (2021)]	9
4	Temperatures used in α_{eff} calculation.	14
5	Dimensions of one single brick.	15
6	Overview over all different used geometries	16
7	Evaluation of a gradient[ANSYS (2023)].	17
8	C_p of brick, c_p and ν of air.	20
9	Plot of ϕ_i/ϕ_i^{ext} for the coarse, medium and fine grid.	23
10	GCI over time.	24
11	Plot of p calculated following Equation(19) over time.	25
12	Plot of R over time.	26
13	Shell conduction model with three layers.	27
14	Emissivity of the brick material over temperature.	28
15	Plane at which the profile is taken	30
16	Temperature, effective alpha, temperature distribution and total heat flux.	35
17	Stream wise velocity profile after each brick.	37
19	Picture of the cut brick.	38
18	Positions in the hole, velocity and temperature along line.	40
20	Contour of the stream wise velocity at the end of the simulation.	42
21	Contour of the temperature at the end of the simulation	43
22	Velocity profiles.	44
22	Velocity profiles.	47

List of Figures

23	Comparison of measured brick temperatures and our simulated brick temperatures at the best fitting measurement point.	50
24	total heat flux over time for all different cases.	58
25	contour of brick temperature at $t=2400s$	61
26	contour of brick temperature at $t=4800s$	63
27	contour of brick temperature at $t=7200s$	65
28	temperature profile after 3 rd brick at $t=7200s$	67

List of Tables

1	Overview of different cases	16
2	Dimensions of the different cases	17
3	Solution Methods	18
4	Used models and solver type	18
5	Material properties	19
6	Cell count and refinement ratio of grid independence study	22
7	Common position and type of used boundary conditions used in all cases	29
8	Mesh metrics.	31
9	Difference compared to the offset case.	36
10	Percentage of the total mass flow passing through the brick	38
11	Comparison of pressure drop and heat transfer coefficient	48

References

- ANSYS, I. (2023). *ANSYS Fluent Theory Guide, Release 2023 R2*. ANSYS, Inc., Canonsburg, USA.
- Celik, I. B., Ghia, U., Roache, P. J., Freitas, C. J., Coleman, H., and Raad, P. E. (2008). Procedure for estimation and reporting of uncertainty due to discretization in cfd applications. *Journal of fluids engineering*, 130(7):78001–078001 (4).
- Ciofalo, M. (2022). *Thermofluid Dynamics of Turbulent Flows : Fundamentals and Modelling*. UNIPA Springer Series. Springer International Publishing Imprint: Springer, Cham, 1st ed. 2022 edition.
- Jeschar, R. (1990). *Grundlagen der Wärmeübertragung*. Viola-Jeschar.
- Mat Ali, M. S., Doolan, C., and Wheatley, V. (2009). Grid convergence study for a two-dimensional simulation of flow around a square cylinder at a low reynolds number. *Seventh International Conference on CFD in the Minerals and Process Industries CSIRO, Melbourne, Australia*, pages 1–6.
- Menter, F. R. (1994). Two-equation eddy-viscosity turbulence models for engineering applications. *AIAA Journal*, 32:1598–1605.
- Menter, F. R. (2009). Review of the shear-stress transport turbulence model experience from an industrial perspective. *International Journal of Computational Fluid Dynamics*, 23(4):305–316.
- Roache, P. J. (1994). Perspective: A method for uniform reporting of grid refinement studies. *Journal of fluids engineering*, 116(3):405–413.
- Schröder, U. (1971). Modellversuche über druckverlust und

- wärmeübergang in gitterförmigen tunnelofenbesatz. *Diss. TU Clausthal.*
- Specht, E. (2014). *Wärme- und Stoffübertragung in der Thermo-
prozessechnik : Grundlagen, Berechnungen, Prozesse.* Edition GWI
- EWI International. Vulkan-Verl., Essen.
- Venkateshan, S. (2021). *Heat Transfer.* Springer International Pub-
lishing Imprint: Springer, Cham, 3rd ed. 2021 edition.
- Vogt, S.; Nover, K. (1991). Zur anwendung von computermodellen
für die auslegung und optimierung von grobkeramischen tunnelöfen.
Ziegelindustrie Int. (1991), 549–556.
- Vogt, S. (2017a). Benefits and boundary conditions of fast firing clay
building products (part 1). *ZI, Ziegelindustrie International/Brick
and Tile Industry International, 5/2017:32–41.*
- Vogt, S. (2017b). Benefits and boundary conditions of fast firing clay
building products (part 2). *ZI, Ziegelindustrie International/Brick
and Tile Industry International, 6/2017:29–38.*
- Vogt, S. (2018). Benefits and boundary conditions of fast firing clay
building products (part 3). *ZI, Ziegelindustrie International/Brick
and Tile Industry International, 1/2018:12–19.*

A Total heat flux over time

Here, the total heat flux over time into one brick is plotted for the different cases, as can be seen in Fig.(24). If two different mass flows are considered, the cases with a larger mass flow of 0.6kg/s start steeper than the cases with, 0.4kg/s which indicates a better heat transfer. Furthermore, the offset case is on par with the smaller case with larger mass flow of 0.6kg/s . This shows that the placement of the bricks onto the kiln has a significant influence on the heat transfer.

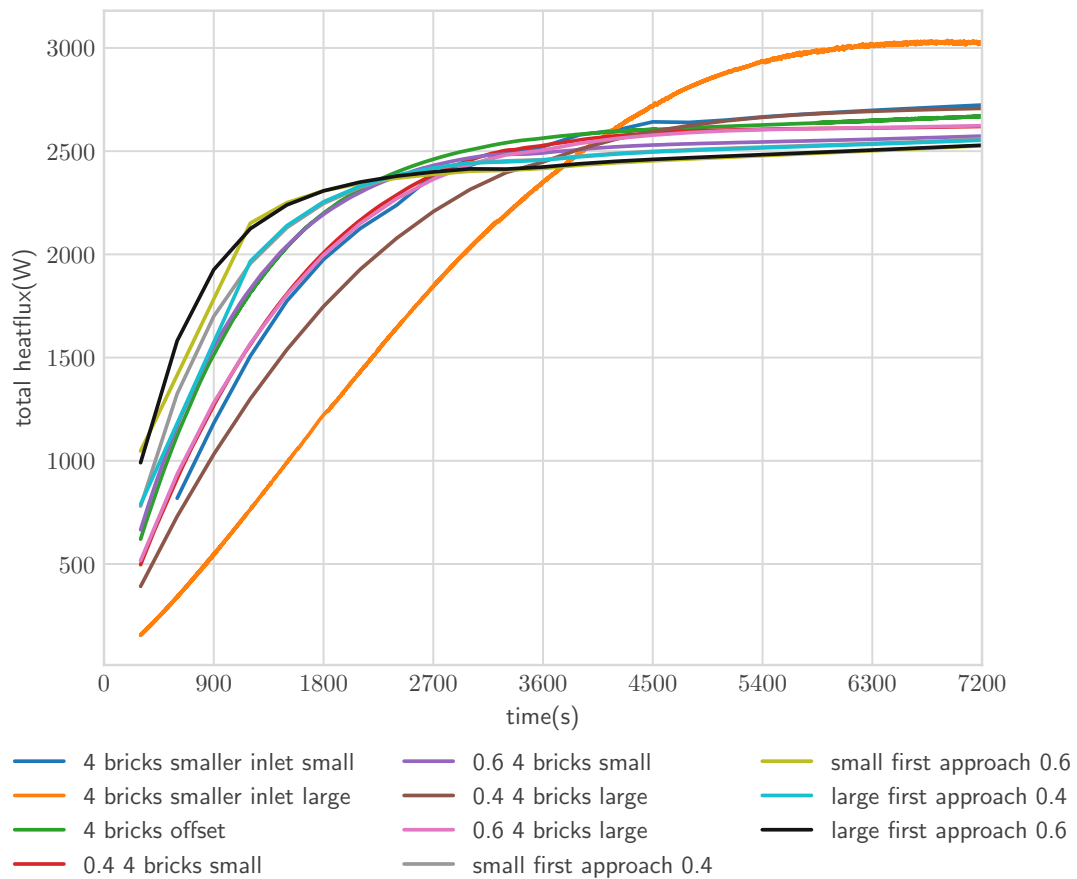
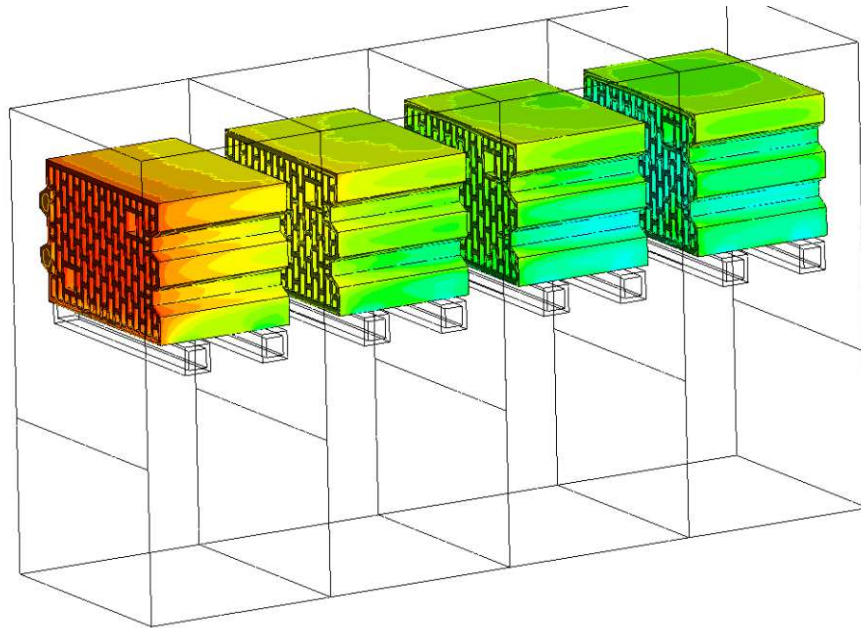


Figure 24: total heat flux over time for all different cases.

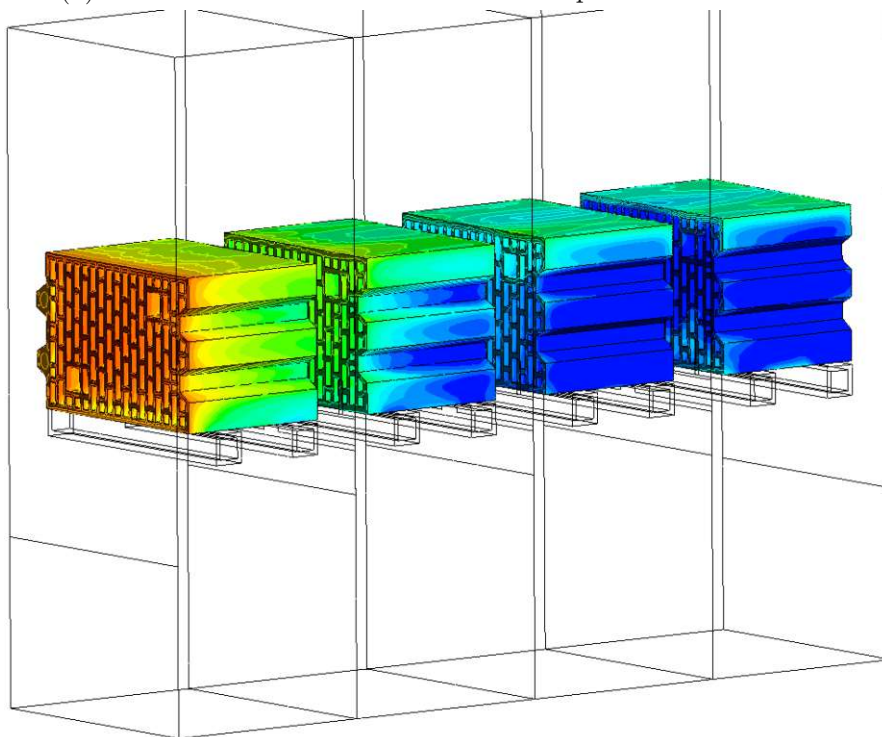
B Temperature contour plots

Here a contour plot of temperature at three different times(2400s, 4800s, 7200s) are shown. One can clearly see that the temperature distribution on the different bricks gets better from the large case to the small case, and the offset case has the most uniform temperature distribution. In Fig.(28) the temperature profile after the third brick is shown. Here, a better temperature distribution in the small and offset case compared to the large case can be observed.

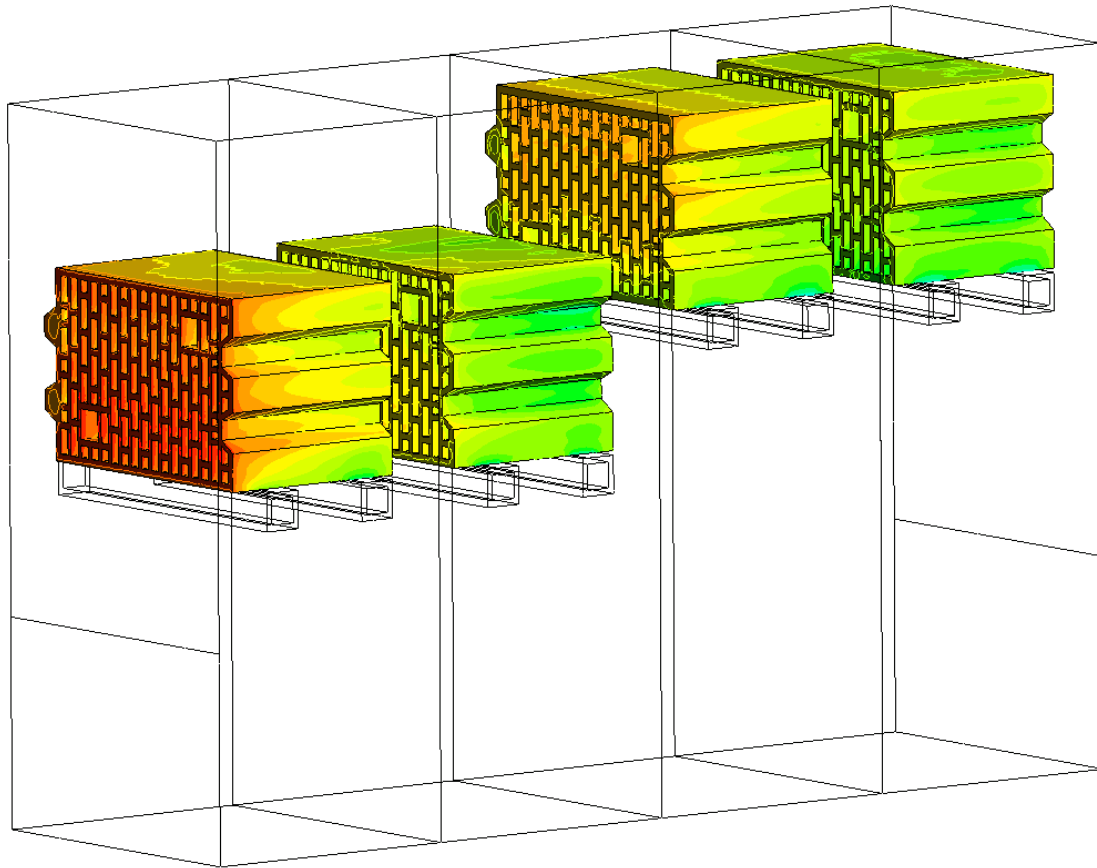
B Temperature contour plots



(a) 4 bricks smaller inlet small brick temperature at $t=2400s$.



(b) 4 bricks smaller inlet large brick temperature at $t=2400s$.



(c) 4 bricks offset brick temperature at $t=2400$ s.

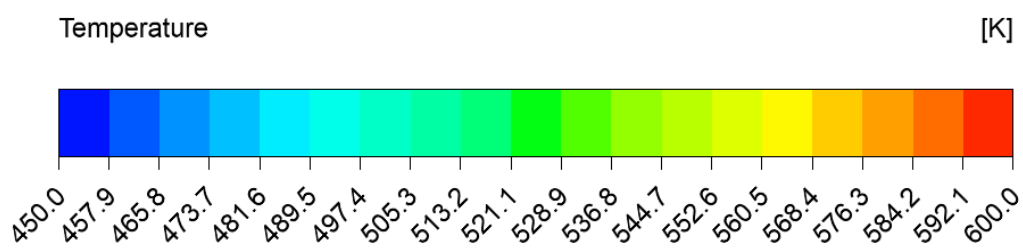
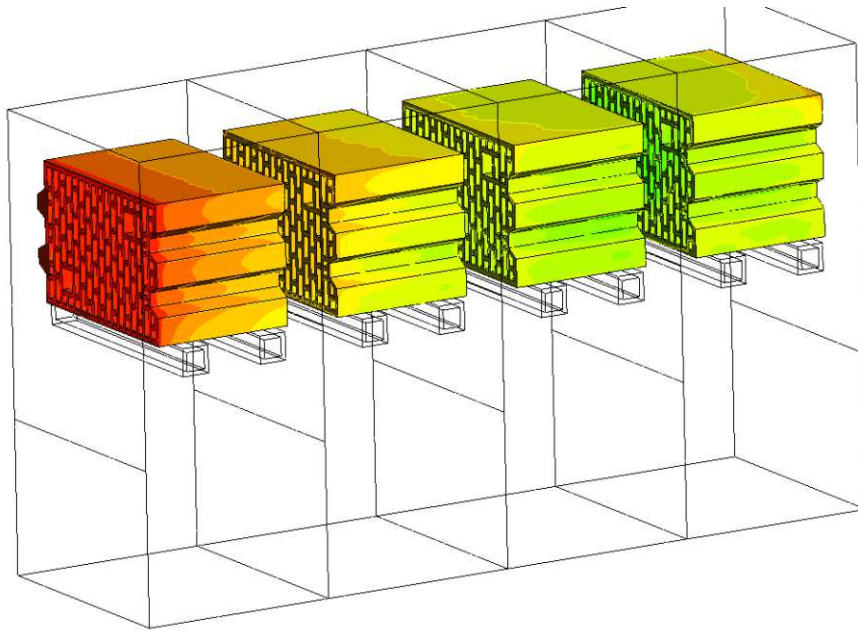
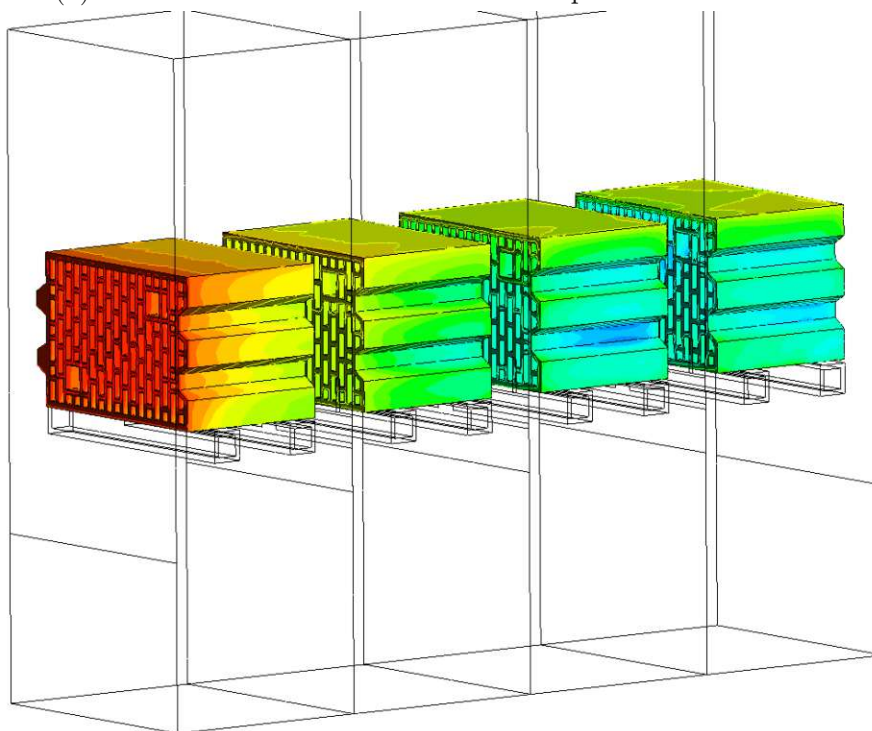


Figure 25: contour of brick temperature at $t=2400$ s.

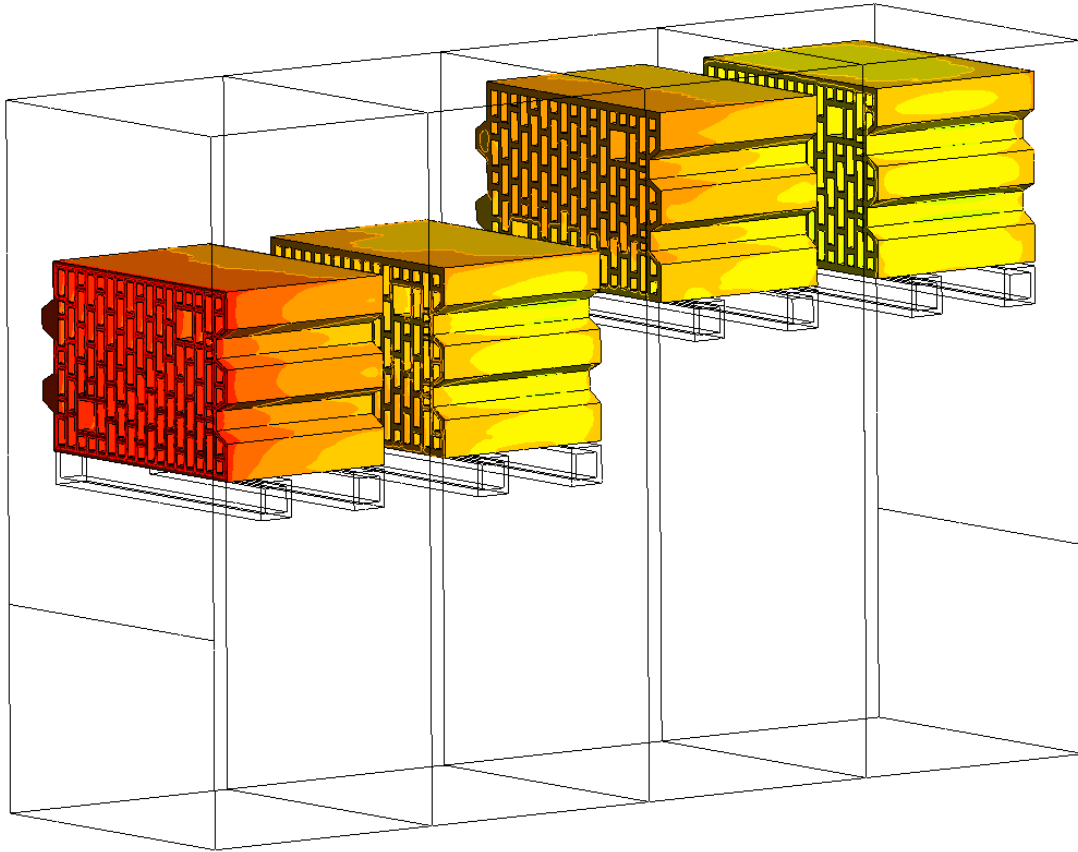
B Temperature contour plots



(a) 4 bricks smaller inlet small brick temperature at $t=4800s$.



(b) 4 bricks smaller inlet large brick temperature at $t=4800s$.



(c) 4 bricks offset brick temperature at $t=4800s$.

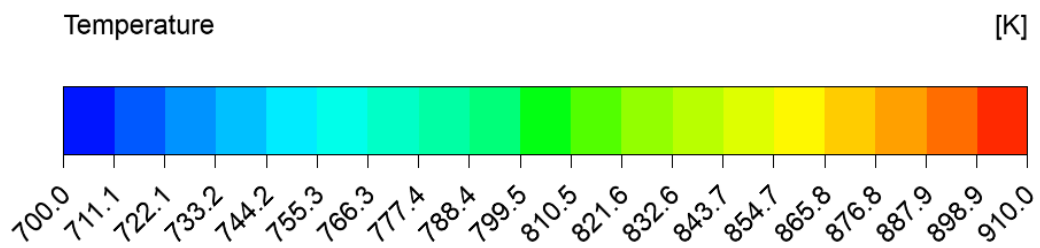
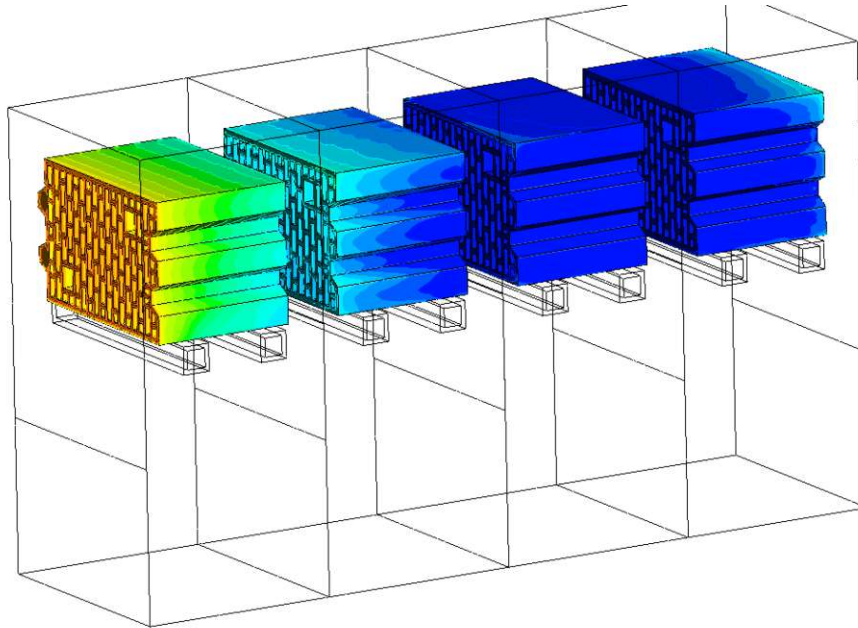
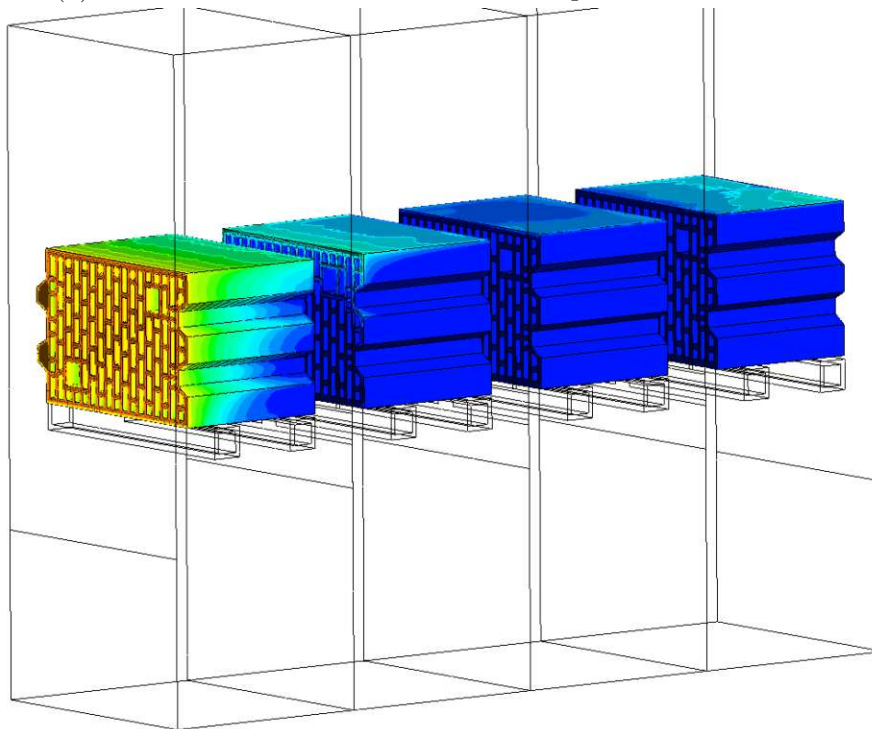


Figure 26: contour of brick temperature at $t=4800s$.

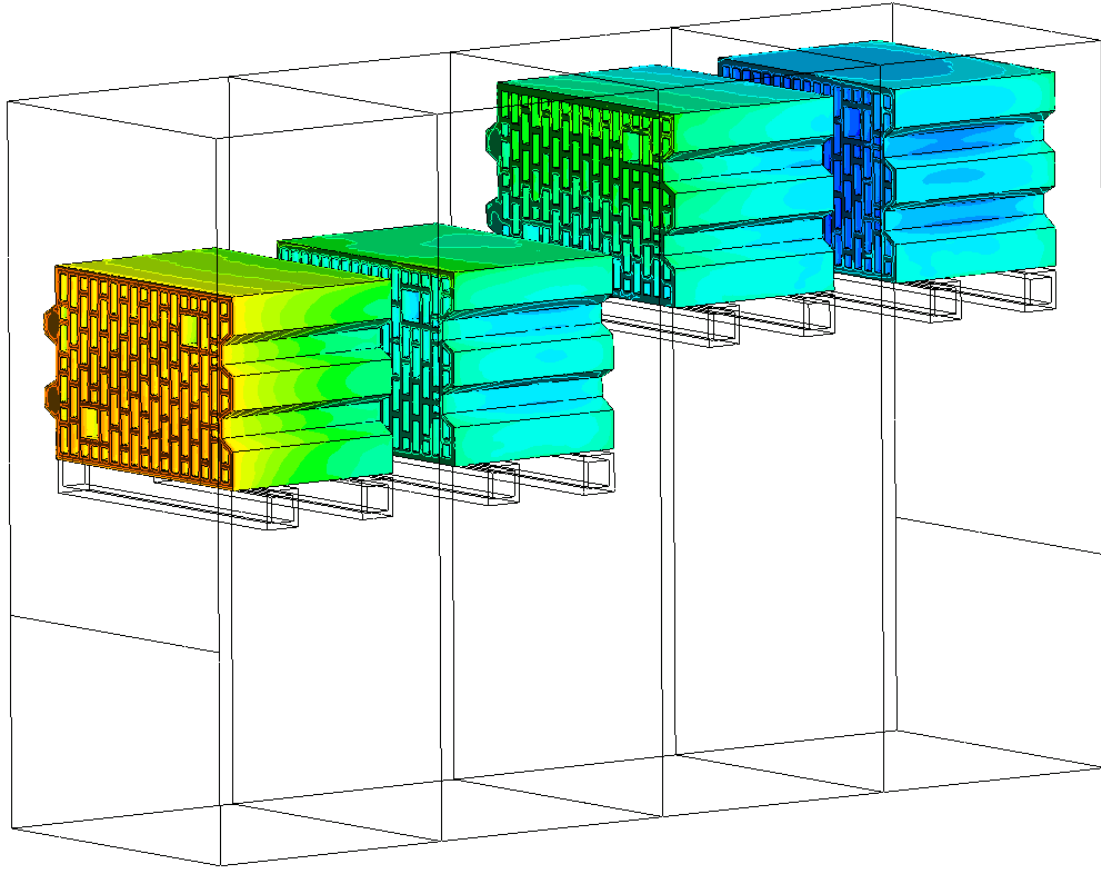
B Temperature contour plots



(a) 4 bricks smaller inlet small brick temperature at $t=7200s$.



(b) 4 bricks smaller inlet large brick temperature at $t=7200s$.



(c) 4 bricks offset brick temperature at $t=7200s$.

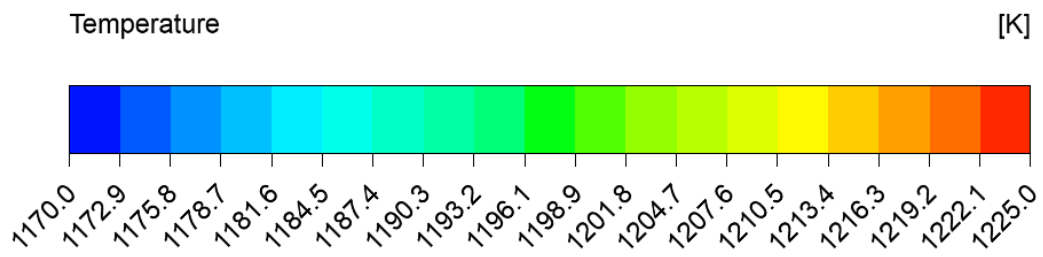
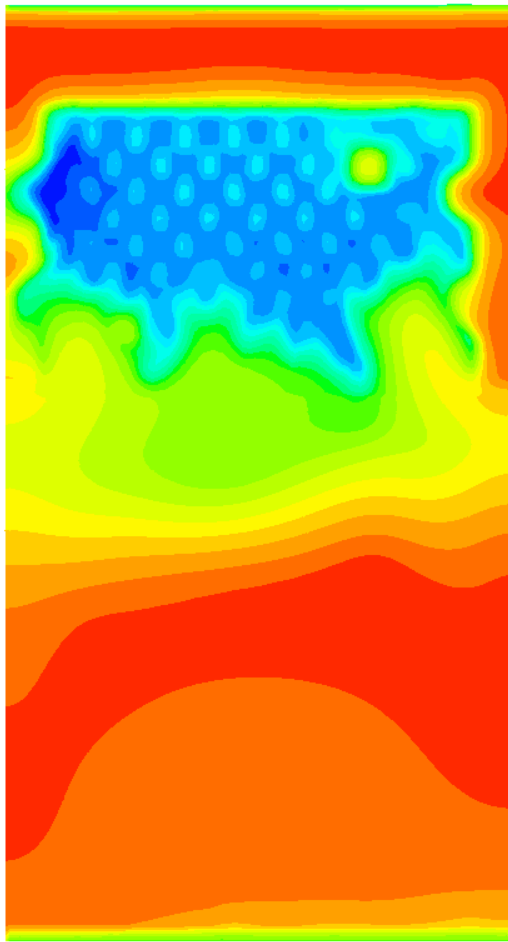
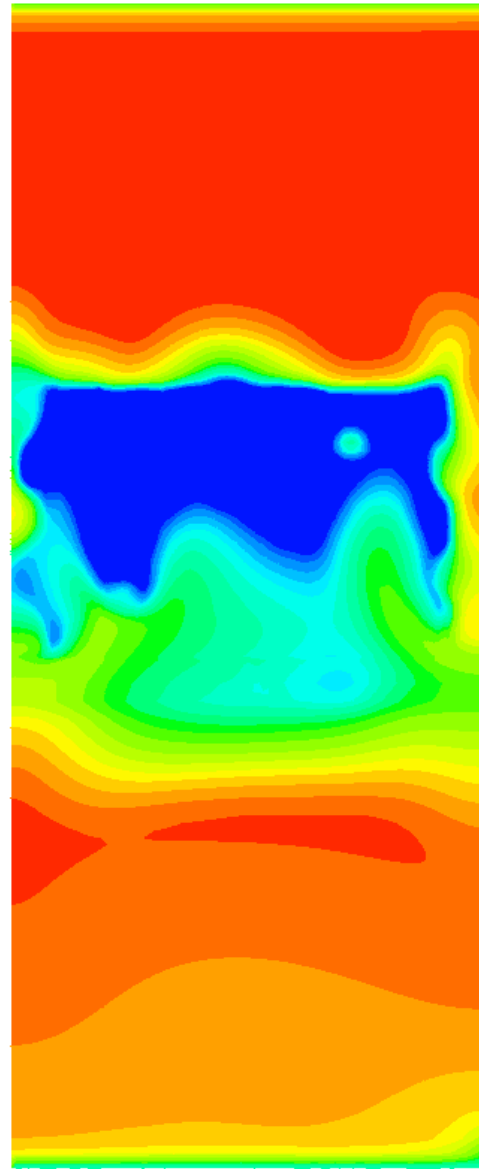


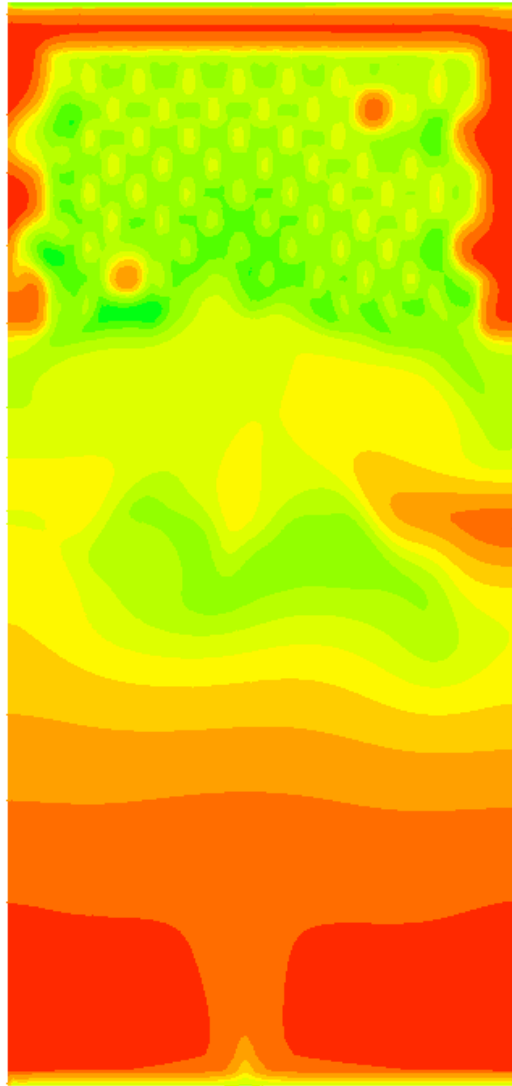
Figure 27: contour of brick temperature at $t=7200s$.



(a) 4 bricks smaller inlet small temperature profile after 3rd brick at $t=7200$ s.



(b) 4 bricks smaller inlet large temperature profile after 3rd brick at $t=7200$ s.



(c) 4 bricks offset temperature profile after 3rd brick at $t=7200s$.

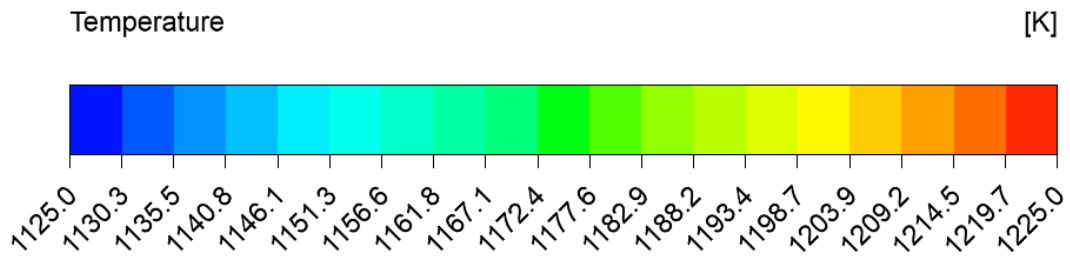


Figure 28: temperature profile after 3rd brick at $t=7200s$.